

# Global Biogeochemical Cycles®









## RESEARCH ARTICLE

10.1029/2022GB007363

## Dissolved Iron Patterns Impacted by Shallow Hydrothermal Sources Along a Transect Through the Tonga-Kermadec Arc

### Key Points:

- Shallow hydrothermal plumes are not transported over long distances, in contrast to what has been previously reported for deep plumes
- Specific surface ocean conditions and chemical processes are primarily responsible for the low dispersion of shallow hydrothermal iron
- Nevertheless, the cumulative impact of multiple sources along the Tonga arc could fertilize the entire Lau Basin with dissolved iron

C. Tilliette<sup>1</sup> , V. Taillandier<sup>1</sup>, P. Bouruet-Aubertot<sup>2</sup>, N. Grima<sup>3</sup>, C. Maes<sup>3</sup> , M. Montanes<sup>1</sup>, G. Sarthou<sup>4</sup>, M.-E. Vorrath<sup>5</sup>, V. Arnone<sup>6</sup> , M. Bressac<sup>1</sup> , D. González-Santana<sup>4</sup> , F. Gazeau<sup>1</sup>, and C. Guieu<sup>1</sup> 

<sup>1</sup>Laboratoire d'Océanographie de Villefranche, Sorbonne Université, CNRS, Villefranche-sur-Mer, France, <sup>2</sup>Laboratoire d'Océanographie et de Climatologie par Expérimentation et Approche Numérique (LOCEAN), Sorbonne Université, CNRS, IRD, Paris, France, <sup>3</sup>Laboratoire d'Océanographie Physique et Spatiale (LOPS, Umr 6523), University Brest, CNRS, IRD, Ifremer, IUEM, Brest, France, <sup>4</sup>University Brest, CNRS, IRD, Ifremer, LEMAR, Plouzane, France, <sup>5</sup>Alfred Wegener Institute, Helmholtz Centre for Polar and Marine Research, Bremerhaven, Germany, <sup>6</sup>Instituto de Oceanografía y Cambio Global, IOCAG, Universidad de Las Palmas de Gran Canaria, ULPGC, Telde, Spain

### Supporting Information:

Supporting Information may be found in the online version of this article.

### Correspondence to:

C. Tilliette and C. Guieu,  
[chloe.tilliette@imev-mer.fr](mailto:chloe.tilliette@imev-mer.fr),  
[cecile.guieu@imev-mer.fr](mailto:cecile.guieu@imev-mer.fr)

### Citation:

Tilliette, C., Taillandier, V., Bouruet-Aubertot, P., Grima, N., Maes, C., Montanes, M., et al. (2022). Dissolved iron patterns impacted by shallow hydrothermal sources along a transect through the Tonga-Kermadec arc. *Global Biogeochemical Cycles*, 36, e2022GB007363. <https://doi.org/10.1029/2022GB007363>

Received 18 FEB 2022

Accepted 29 JUN 2022

**Abstract** In the Western Tropical South Pacific, a hotspot of dinitrogen-fixing organisms has been identified. The survival of these species depends on the availability of dissolved iron (DFe); however, the source of this DFe is still unclear. DFe was measured along a transect from 175°E to 166°W near 19–21°S. The distribution of DFe showed high spatial variability: low concentrations (~0.2 nmol kg<sup>-1</sup>) in the South Pacific gyre and high concentrations (up to 50 nmol kg<sup>-1</sup>) in the west of the Tonga arc, indicating that this arc is a clear boundary between iron-poor and iron-rich waters. An optimal multiparameter analysis was used to distinguish the relative importance of physical transport relative to non-conservative processes on the observed distribution. This analysis demonstrated that the shallow hydrothermal sources present along the Tonga-Kermadec arc are responsible for the high concentrations observed in the photic layer. Nevertheless, in contrast to what has been observed for deep hydrothermal plumes, our results highlighted the rapid decrease in DFe concentrations near shallow hydrothermal sources. This is likely due to a shorter residence time of surface water masses combined with several biogeochemical processes at play (precipitation, scavenging, biological uptake, and photoreduction). This study clearly highlights the role of shallow hydrothermal sources on the DFe cycle within the Tonga-Kermadec arc where a strong link to biological activity in surface waters can be assessed, despite the small but significant fraction of DFe ultimately stabilized. It also emphasizes the need to consider the impact of these sources for a better understanding of the global iron cycle.

## 1. Introduction

Iron (Fe) is the fourth most abundant element in the Earth's crust (about 6.7%; Rudnick & Gao, 2003) but it is present at sub-nanomolar concentrations in seawater (<10<sup>-9</sup> mol L<sup>-1</sup>; Johnson et al., 1997). Yet, Fe is a key micronutrient for the growth and metabolism of all living organisms and especially phytoplankton for which it is essential for the proper functioning of the photosynthetic system (Behrenfeld & Milligan, 2013; Raven et al., 1999). Consequently, Fe has a direct influence on primary production (Martin et al., 1994; Sunda & Huntsman, 1995) and thus plays an important role on carbon export and sequestration in the ocean interior (Martin, 1990). Numerous natural fertilization studies have investigated the importance of iron, primarily in the Southern Ocean (Blain et al., 2007; Pollard et al., 2007), and have reported enhanced primary production rates and particulate organic carbon export efficiencies, which may influence the biological carbon pump (Morris & Charette, 2013). In the context of climate change (IPCC, 2021), characterizing the elements governing the efficiency of this pump is of great interest. Due to its importance, the number of dissolved Fe (DFe) concentration measurements has increased impressively in recent years thanks to the GEOTRACES program (<https://www.geotraces.org/>), particularly in the deep ocean. However, there is still a lack of data for some key ocean regions, such as the Western Tropical South Pacific (WTSP) Ocean.

The WTSP Ocean (160°E–160°W) has recently been identified as a hotspot of dinitrogen (N<sub>2</sub>) fixation with some of the highest rates recorded in the global ocean (Bonnet et al., 2017). Diazotrophy is a process favored in phosphorus-rich, nitrogen-poor waters, that fuels the ocean with new nitrogen, helping to maintain ocean productivity and carbon sequestration (Caffin et al., 2018). This region is characterized by two biogeochemical

© 2022. The Authors.

This is an open access article under the terms of the [Creative Commons Attribution License](https://creativecommons.org/licenses/by/4.0/), which permits use, distribution and reproduction in any medium, provided the original work is properly cited.

subregions separated by the Tonga-Kermadec arc: (a) the South Pacific gyre located east of the arc and characterized by low  $N_2$  fixation rates ( $\sim 85 \mu\text{mol N m}^{-2} \text{d}^{-1}$ ) despite sufficient phosphate availability ( $0.11 \mu\text{mol L}^{-1}$ ; Moutin et al., 2008) and (b) the Melanesian archipelago together with the Lau Basin located west of the arc and characterized by high  $N_2$  fixation rates ( $\sim 631 \mu\text{mol N m}^{-2} \text{d}^{-1}$ ; Bonnet et al., 2018). This spatial decoupling of  $N_2$  fixation has been attributed to the alleviation of DFe limitation in the Melanesian archipelago (up to  $60 \text{ nmol L}^{-1}$  in the photic layer; Guieu et al., 2018) in contrast to the DFe-poor waters of the South Pacific gyre (Bonnet et al., 2008; Mills et al., 2004), with the Tonga-Kermadec arc acting as a barrier separating these two biogeochemical provinces.

However, the question of the iron origin in the WTSP Ocean remains open. Multiple external sources of iron may be good candidates to explain iron availability in Melanesian waters. These sources include potential sediment-derived iron inputs in the shallower waters of the arc, especially near the islands (Dutheil et al., 2018; Homoky et al., 2016; Raapoto et al., 2019). Similarly, the WTSP Ocean is surrounded by numerous ferromagnesian islands that may supply many terrigenous nutrients, including iron, through runoff from island slopes (Shiozaki et al., 2014). Other good candidates are atmospheric iron inputs emitted from the many subaerial volcanoes hosted by the WTSP Ocean. However, these were quantified during the OUTPACE cruise (Moutin & Bonnet, 2015) and Guieu et al. (2018) stated that they were too low to explain the DFe concentrations measured in the region. Another possibility is that DFe may be supplied by water masses of remote origin entering this region (Mahadevan, 2016), therefore the role of physical transport must be also considered. Finally, deep mid-ridge hydrothermal sources are known to be major sources of DFe for the deep ocean (German et al., 2016). Hydrothermal inputs are also documented at much shallower depths in the region (Massoth et al., 2007) and the hypothesis that the high DFe concentrations measured in the WTSP photic layer (0–150 m) come from shallow hydrothermal sources was proposed by Guieu et al. (2018). The latter two hypotheses appear to be the most compelling and will be explored in detail in this work.

To understand the sources and sinks affecting the DFe distribution in the WTSP Ocean, we first present the DFe concentrations measured along a 6,100 km transect near  $\sim 20^\circ\text{S}$  (Guieu & Bonnet, 2019, Figure 1a). We then introduce the theoretical distribution of DFe using a water mass analysis. The anomalies between theoretical and measured DFe concentrations are then discussed to highlight the potential hydrothermal origin of DFe in the Lau Basin. Finally, the different processes involved are discussed to explain the longitudinal evolution of DFe within the study transect.

## 2. Materials and Methods

### 2.1. Oceanographic Campaign Presentation and Sampling

The present study was conducted as part of the TONGA cruise (GPpr14; Guieu & Bonnet, 2019) that took place onboard the R/V L'Atalante from 31 October to 5 December 2019, along a transect extending from New Caledonia to the western end of the South Pacific gyre. This 6,100 km-long transect allowed the characterization of two biogeochemical zones of the region separated by the Tonga-Kermadec arc (Figure 1). The objective of the cruise was to investigate the impact of shallow hydrothermal inputs on biogeochemical cycles, particularly trace metal cycles, downward export, and planktonic communities.

*Investigated stations.* Two types of stations were sampled: (a) nine short-duration stations (SD 1, 2, 3, 4, 6, 7, 8, 11, and 12) dedicated to biogeochemical sampling through water column vertical casts and (b) two long-duration stations (LD 5 and 10) dedicated to the study of the impacts of hydrothermal fluids from two identified shallow sources along a short  $\sim 17$  km transect including 5 substations, named from T5 to T1, with T5 being the closest to the hydrothermal source. For these two long-duration stations, hydrothermal sources were detected from the acoustic anomalies (see Figure S2 in Supporting Information S1) on small caldera-like structures using a multibeam echosounder (hull-mounted EM-710 echosounder of R/V L'Atalante, operating at a frequency of 70–100 kHz for depths  $< 1,000$  m). The two T5 substations were positioned where the highest acoustic anomalies were recorded and the calderas of LD 5 and 10 were identified at 200 and 300 m, respectively. Both for LD 5 and LD 10, "T1" substations were positioned west of "T5" (consistent with the main surface current direction) as soon as the seafloor was at  $\sim 2,000$  m (allowing the deployment of a drifting mooring line). Between T1 and T5, additional stations were staged to investigate the longitudinal impact of hydrothermal fluids released from T5. Following the eruption of New Late'iki (i.e., Metis Shoal;  $19.18^\circ\text{S}$ ,  $174.87^\circ\text{W}$ ) one month prior to the cruise

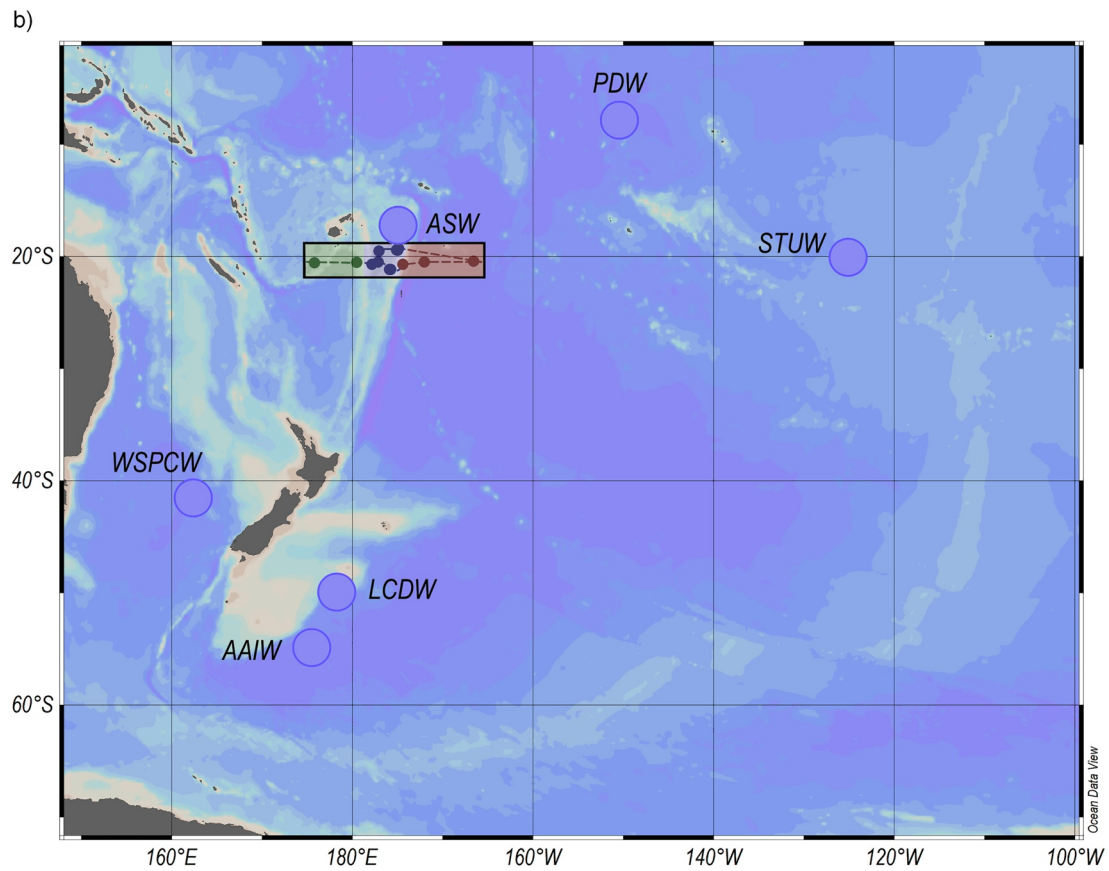
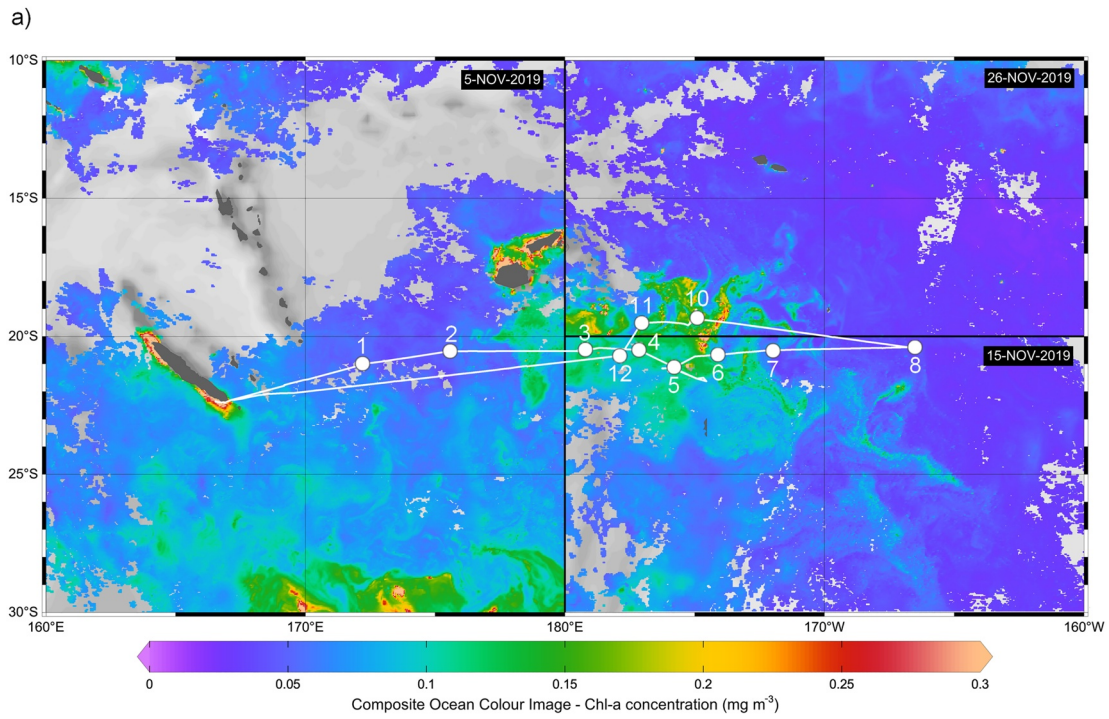


Figure 1.

(a submarine volcano that turned into an island; Plank et al., 2020), an additional substation “Proxnov” located further north of this site (15 km from LD 10-T5) was studied as part of LD 10.

*CTD sampling.* Temperature, conductivity (salinity), pressure (depth), and dissolved oxygen vertical profiles were obtained using a rosette-mounted CTD SeaBird SBE 911 Plus sensor. At each station, conventional CTD casts were conducted to sample for inorganic nutrients using a rosette equipped with 24 Niskin bottles (12 L) and trace-metal clean rosette (TMR) casts were performed for dissolved and particulate trace metal sampling (see Section 2.2). A total of 398 samples were collected for DFe analyses. Inorganic nutrients (nitrate:  $\text{NO}_3^-$ , phosphate:  $\text{PO}_4^{3-}$ , and silicate:  $\text{Si}(\text{OH})_4$ ) were measured as detailed in Bonnet et al. (2018).

*Autonomous platforms.* Several autonomous instruments were deployed during the cruise at stations LD 5-T1 and T5, SD 11 and SD 12. Drifter observations were thus possible at the surface (0–15 m) through the deployment of Surface Velocity Program (SVP) drifters with the following WMO-id at stations SD 12 (5,501,635, 5,501,636, 5,501,637, 5,501,638, and 5,501,639), LD 5-T1 (4,101,779, 4,402,504, 5,102,720, 5,102,721, and 6,301,680), and LD 5-T5 (5,501,630, 5,501,631, 5,501,632, 5,501,633, and 5,501,634; <http://www.coriolis.eu.org/Data-Products/Data-Delivery/Data-selection>) and at depth (1,000–1,500 m) through the deployment of deep Argo autonomous floats (<https://fleetmonitoring.euro-argo.eu/dashboard>) at stations LD 5-T1 (6,903,025), LD 5-T5 (6,902,985), SD 11 (6,902,989), and SD 12 (6,902,927). The short trajectory (5 days, 0–1,000 m) of the drifting mooring line deployed at LD 5-T1 could also be observed.

## 2.2. Dissolved Iron Measurements

All handling was performed under ultra-clean conditions (Bruland et al., 1979) following the guidelines established by the GEOTRACES cookbook (Cutter et al., 2017).

*Preparation of the sampling material.* All collecting material used was previously washed following a rigorous procedure. Nalgene® 60 mL low-density polyethylene bottles were first immersed in a surfactant bath (2% v/v, Decon™) for one week before being rinsed 3-times with MilliQ water (resistivity  $>18.5 \text{ M}\Omega \text{ cm}^{-1}$ ). Bottles were then immersed in a Suprapure hydrochloric acid solution (HCl, Supelco®; 10% v/v) for one month before being rinsed again 3-times with MilliQ water. Vials were finally one-third filled with 1% v/v Ultrapure HCl (Supelco®) and stored double-bagged pending use.

*Sampling and storage of seawater samples.* During the cruise, seawater samples were collected using GO-FLO bottles mounted on a TMR (General Oceanics Inc., Model 1,018 Intelligent Rosette) attached to a 6 mm Kevlar line. Immediately after recovery, the rosette was transferred into a clean container for sampling. Bottles were pressurized with 0.2  $\mu\text{m}$ -filtered nitrogen (Air Liquide®) allowing in-line filtration using an acid-cleaned 0.45  $\mu\text{m}$  polyethersulfone filter (Supor®). Acid-cleaned bottles were rinsed 3-times with sampled seawater before final collection. Collected samples were acidified to pH  $\sim 1.7$  with Ultrapure HCl (0.2% v/v, Supelco®) within 24 hr of collection and stored double-bagged pending analysis.

*Dissolved iron analysis in seawater.* Samples for DFe were analyzed in a clean room by flow injection and chemiluminescence detection (FIA-CL) at the Laboratoire d’Océanographie de Villefranche, as described by Blain et al. (2008) and adapted from the protocol originally described by Obata et al. (1993). Some improvements have been made compared to the last protocol. First, a new 8-hydroxyquinoline (8-HQ) resin was produced according to the protocol of Landing et al. (1986) where 8-HQ was immobilized on Fractogel TSK HW75-F (Tosoh Biosciences). The column was manufactured as described by Bowie et al. (1998) (i.e., the resin was placed in a rigid Teflon™ tube and isolated with clean quartz wool). Prior to each analysis day, two successive purifications of luminol on the 8-HQ resin were performed first on the pure luminol solution and then on the diluted solution. In addition, storage of the luminol solution in an opaque package significantly improved its shelf life and dosage

**Figure 1.** (a) Transect of the cruise superimposed on surface chlorophyll-*a* concentrations ( $\text{mg m}^{-3}$ ). Different oceanic regions were occupied during the cruise: Melanesian waters including short duration (SD) stations 1, 2, and 3, Lau Basin including SD 4, 11, and 12 as well as long duration (LD) stations 5 and 10, and the South Pacific gyre including SD 6, 7, and 8. Within each subregion are represented the chlorophyll-*a* concentrations observed over three time periods corresponding to the mean date of occupancy: 5 November 2019 for the western part of the transect, 15 November for the southeastern part, and 29 November for the northeastern part. (b) Bathymetric map of the South Pacific Ocean showing the transect of the cruise (small dots) and the location at which the end-members were defined (large blue dots). The frames around the transect represent the different subregions studied during the cruise: green for the Melanesian waters, blue for the Lau Basin, and red for the South Pacific Gyre. Higher resolution bathymetric maps focusing on the cruise transect and including the two smaller transects conducted at the long-duration stations LD 5 and LD 10 are available in Figure S1 in Supporting Information S1. See Table 1 for end-members acronyms.

reproducibility. Finally, the occasionally observed loss of sensitivity was resolved thanks to a 15-min diluted aqua regia flush (0.16 M HNO<sub>3</sub><sup>-</sup>, 0.6 M HCl) performed every two analysis days to remove organics likely accumulated in the 8-HQ system that could not be eliminated by HCl alone.

Apart from these points, the method remained the same as in Blain et al. (2008). Briefly, the analysis was performed in a closed circuit, which implied no external manipulation and minimized contamination risk. All tubes used in the analytical system were made of Teflon™ except the Tygon™ tubes used for the peristaltic pump. Since 8-HQ selectively chelates DFe at pH 5, the pH of the samples was adjusted to 5 by adding Ultrapure ammonia (20%–22%, Ultrex II, J.T. Baker©) and a 3-times purified ammonium acetate buffer. Samples were then pre-concentrated on an 8-HQ chelating resin for 120 s. The chelated DFe was eluted with Suprapure HCl (0.7 M) and mixed with luminol (0.74 M), ammonia (1 M), and hydrogen peroxide (0.7 M). The luminescent reaction product was detected by a photomultiplier at the end of the circuit. Given the wide range of measured DFe concentrations ([DFe]), the calibration curves were adapted to measure [DFe], up to 2 nM for most samples. The DFe-rich samples were diluted up to 1:20 depending on the concentration in a poor-DFe seawater collected at SD 8 also used as an in-house standard (DFe = 0.38 ± 0.03 nM, n = 26). The final concentration of those diluted samples did not exceed 5 nM and a 0–5 nM calibration curve was used in that case.

*Validation of the measurements.* Analytical blanks (i.e., reagent and manifold), calibration lines, and reference material values were determined each analysis day and are reported in Table S1 in Supporting Information S1. The mean analytical blank, calculated from the daily determinations with MilliQ water (n = 19), was 21 ± 22 p.m. and the detection limit (i.e., three times the standard deviation on the manifold blank divided by the calibration slope) was 16 ± 7 p.m. Each sample was analyzed in triplicate. Method accuracy was evaluated daily by analyzing the GEOTRACES Surface (GS) seawater standard after each calibration and every 5–10 samples to validate measurements and monitor analytical stability. An in-house standard, whose concentration was previously determined by repeated analyses (n = 26) cross-calibrated with the GS standard, was also measured with the samples as an additional quality control. GS standard analyses for DFe averaged 0.510 ± 0.046 nM (n = 24) which compares well with community consensus concentrations of 0.546 ± 0.046 nM. It has to be noted that additional verifications were performed to ensure the accuracy and reproducibility of the method and are reported in Table S1 in Supporting Information S1. All volumetric concentrations were converted to nmol kg<sup>-1</sup> based on temperature and salinity data measured at each station and sampling depth.

### 2.3. Water Mass Analysis

An optimum multiparameter analysis (OMP) was used to resolve the water mass structure along the cruise transect (Tomczak, 1999) and subsequently to assess DFe anomalies. This method determines an optimal least squares solution of a linear model of mixing equations to solve the contribution of selected water masses (i.e., end-members) as a function of a range of hydrographic parameters. In the equational system, the end-member contributions are used as variables and the hydrographic properties as parameters. In this work, the available parameters are temperature (T), salinity (S), concentrations of dissolved oxygen (O<sub>2</sub>), nitrate (NO<sub>3</sub><sup>-</sup>), phosphate (PO<sub>4</sub><sup>3-</sup>), and silicic acid (Si(OH)<sub>4</sub>). However, the system is solved by assuming that all parameters are conservative (i.e., there is no sink or source in the ocean interior). This is not acceptable in our case as the selected end-members (see Section 2.3.3) are distributed throughout the South Pacific where nutrients may be consumed through biological uptake and produced through organic matter remineralization and are, by definition, non-conservative. To account for these biogeochemical processes, an extended OMP (eOMP) was performed using the quasi-conservative parameters NO, PO, and SiO for which remineralization or biological uptake have no effect (Broecker, 1974):

$$PO = [O_2] + R_{O_2/P} * [PO_4^{3-}] \quad (1)$$

$$NO = [O_2] + R_{O_2/N} * [NO_3^-] \quad (2)$$

$$SiO = [O_2] + R_{O_2/Si} * [Si(OH)_4] \quad (3)$$

where  $R_{O_2/P}$ ,  $R_{O_2/N}$ , and  $R_{O_2/Si}$  are the Redfield ratios that estimate the number of O<sub>2</sub> moles consumed for 1 mol of PO<sub>4</sub><sup>3-</sup>, NO<sub>3</sub><sup>-</sup> and Si(OH)<sub>4</sub> released during the process of organic matter remineralization, respectively. We

assumed a  $R_{O_2/P} = 155$  (Anderson & Sarmiento, 1994),  $R_{O_2/N} = 9.68$  (Broecker, 1974; Peters et al., 2018), and  $R_{O_2/Si} = 10.33$  (Redfield et al., 1963). This led to the following constraint equations:

$$x_1T_1 + x_2T_2 + \dots + x_nT_n = T_{\text{sample}} + \varepsilon_T \quad (4)$$

$$x_1S_1 + x_2S_2 + \dots + x_nS_n = S_{\text{sample}} + \varepsilon_S \quad (5)$$

$$x_1PO_1 + x_2PO_2 + \dots + x_nPO_n = PO_{\text{sample}} + \varepsilon_{PO} \quad (6)$$

$$x_1NO_1 + x_2NO_2 + \dots + x_nNO_n = NO_{\text{sample}} + \varepsilon_{NO} \quad (7)$$

$$x_1SiO_1 + x_2SiO_2 + \dots + x_nSiO_n = SiO_{\text{sample}} + \varepsilon_{SiO} \quad (8)$$

$$x_1 + x_2 + \dots + x_n = 1 + \varepsilon_x \quad (9)$$

$$x_i \geq 0 \quad (10)$$

where  $x_n$  denotes the contribution of the  $n$ th end-member and  $\varepsilon$  refers to residual values that account for both measurement error and uncertainty in the assignment of end-member properties.

### 2.3.1. Overdetermined System

The eOMP must be realized as an overdetermined system, which means that the number of end-members must be strictly inferior to the number of parameters. We defined six end-members contributing to the cruise transect (see Section 2.3.3) but only five parameters were available (T, S, NO, PO, and SiO). The transect was therefore divided into two vertical domains in which the eOMP was performed independently, as it has been done in previous studies (e.g., Artigue et al., 2020; Fitzsimmons et al., 2016): (a) an upper domain comprising depths from 100 to 1,000 m (density from  $23.8 \text{ kg m}^{-3}$  to  $26.8 \text{ kg m}^{-3}$ ) and (b) a lower domain comprising depths from 1,000 m to the seafloor ( $>26.8 \text{ kg m}^{-3}$ ). The eOMP was performed using the OMP v2.0 MatLab package developed by Johannes Karstensen and Matthias Tomczak (<https://omp.geomar.de/>).

### 2.3.2. Upper Layer Inclusion

To consider depths including shallow sources (0–200 m) in the analysis although the parameters (PO, NO, and SiO) could not be considered as conservative due to potential biological uptake, an artificial water mass called Artificial Surface Water (ASW) was created using salinity data obtained during the cruise at  $\sim 100$  m. The surface layer part included in eOMP was selected when acceptable residuals were obtained ( $<5\%$ ), leading to the exclusion of water masses above 100 m ( $<23.8 \text{ kg m}^{-3}$ ). Since the excluded area is the area of maximum interest for surface communities, the inferred water mass contributions and DFe anomalies in the layer between 100 and 200 m (lower surface layer) were assumed not to be affected by biological processes.

### 2.3.3. End-Member Selection and Data Acquisition

End-member identification was performed based on hydrographic properties (potential density anomaly, salinity, oxygen, and nitrate concentrations) observed along the transect profiles (Figure S3 in Supporting Information S1) and the boundaries of each end-member zone were carefully defined by a thorough review of the literature. To present “pure” characteristics, end-member properties (Table 1) were selected from the core of the water masses from several databases (World Ocean Atlas, GLODAP, and World Ocean Circulation Experiment) but were also found in the literature (Blain et al., 2008; Loscher et al., 1997; Tagliabue et al., 2012). End-members [DFe] were estimated using the GEOTRACES database. As the South Pacific is largely undersampled, especially for metals, only one data point was available for the Antarctic Intermediate Water (AAIW). For quality purposes, more data ( $n = 85$ ) were found in the Antarctic Circumpolar Current where AAIW flows before reaching Tasmanian waters (Bostock et al., 2013) and resulted in a more accurate value for AAIW from  $0.478 \pm 0.000 \text{ nmol kg}^{-1}$  ( $n = 1$ ) to  $0.426 \pm 0.123 \text{ nmol kg}^{-1}$  ( $n = 86$ ). It should be noted that the assignment of [DFe] to different water masses assumes that DFe behaves conservatively. This represents a caveat in the present study as sources (e.g., hydrothermalism, remineralization, and shelf-platform interactions) and sinks (e.g., scavenging and biological uptake)

**Table 1**  
*End-Members Characteristics (Value ± Uncertainty) Used for the Extended OMP*

Acronym	Water mass name	T (°C)	S	[O <sub>2</sub> ] (μmol kg <sup>-1</sup> )	[PO <sub>4</sub> ] <sup>-</sup> (μmol kg <sup>-1</sup> )	[NO <sub>3</sub> ] <sup>-</sup> (μmol kg <sup>-1</sup> )	[Si(OH) <sub>4</sub> ] (μmol kg <sup>-1</sup> )	"PO" (μmol kg <sup>-1</sup> )	"NO" (μmol kg <sup>-1</sup> )	"SiO" (μmol kg <sup>-1</sup> )	[DFe] (nmol kg <sup>-1</sup> )	Data source
ASW	Artificial Surface Water	24.000 ±0.750 <i>n</i> = 29	34.450 ±0.020 <i>n</i> = 29	210.000 ±8.700 <i>n</i> = 29	0.100 ±0.100 <i>n</i> = 12	0.000 ±0.610 <i>n</i> = 12	1.000 ±0.550 <i>n</i> = 13	225.500 ±24.200	210.000 ±14.604	220.330 ±14.381	0.180 ±0.030 <i>n</i> = 9	TONGA cruise, all stations, November 2019, 19–21°S, 175°E–165°W, 100 m
STUW	Subtropical Underwater	24.464 ±0.833 <i>n</i> = 27	36.299 ±0.136 <i>n</i> = 21	208.535 ±5.040 <i>n</i> = 28	0.177 ±0.030 <i>n</i> = 35	0.117 ±0.078 <i>n</i> = 21	1.416 ±0.260 <i>n</i> = 28	235.984 ±9.619	209.669 ±5.797	223.171 ±7.732	0.134 ±0.018 <i>n</i> = 8	World Ocean Atlas, World Ocean Circulation Experiment, Blain et al. (2008), 18–22°S, 115–135°W, 20–170 m
WSPCW	Western South Pacific Central Water	10.612 ±0.994 <i>n</i> = 241	34.886 ±0.037 <i>n</i> = 248	223.926 ±12.560 <i>n</i> = 236	0.915 ±0.172 <i>n</i> = 233	9.734 ±4.113 <i>n</i> = 212	5.839 ±1.97 <i>n</i> = 232	365.757 ±39.215	318.15 ±52.375	284.247 ±32.959	0.440 ±0.123 <i>n</i> = 19	GEOTRACES GPY01, World Ocean Atlas, World Ocean Circulation Experiment, 39–43°S, 155–175°E, 250–500 m
AAIW	Antarctic Intermediate Water	4.317 ±0.583 <i>n</i> = 96	34.258 ±0.037 <i>n</i> = 100	232.836 ±17.416 <i>n</i> = 73	1.924 ±0.143 <i>n</i> = 76	28.533 ±2.104 <i>n</i> = 65	24.486 ±6.538 <i>n</i> = 52	531.076 ±39.522	509.034 ±37.78	485.786 ±84.959	0.426 ±0.123 <i>n</i> = 86	GEOTRACES GPY01-06, World Ocean Atlas, World Ocean Circulation Experiment, 53–57°S, 170°E–180°W, 500–1,000 m
PDW	Pacific Deep Water	1.952 ±0.142 <i>n</i> = 171	34.662 ±0.011 <i>n</i> = 170	127.324 ±11.914 <i>n</i> = 171	2.713 ±0.090 <i>n</i> = 171	37.488 ±0.977 <i>n</i> = 171	140.151 ±6.558 <i>n</i> = 171	547.808 ±25.801	490.206 ±21.371	1,575.087 ±79.662	0.607 ±0.072 <i>n</i> = 106	GEOTRACES GP16, World Ocean Atlas, World Ocean Circulation Experiment, 7–11°S, 160–140°W, 2,000–3,000 m
LCDW	Lower Circumpolar Deep Water	0.914 ±0.061 <i>n</i> = 116	34.705 ±0.003 <i>n</i> = 117	209.459 ±1.731 <i>n</i> = 108	2.133 ±0.062 <i>n</i> = 113	32.118 ±0.203 <i>n</i> = 114	121.569 ±1.885 <i>n</i> = 113	540.061 ±11.291	520.365 ±3.700	1,465.274 ±14.381	0.635 ±0.178 <i>n</i> = 8	World Ocean Atlas, World Ocean Circulation Experiment, Loscher et al. (1997), Tagliabue et al. (2012), 48–52°S, 172°E–168°W, 4,000–5,000 m

of DFe may have a potential impact on its concentrations as the water masses travel to the study region. This may slightly affect the anomalies derived from this analysis.

#### 2.3.4. Parameters Weighting

Parameters were weighted according to their signal-to-noise ratios (measurement accuracy) and conservative nature (conservative or quasi-conservative). The highest weight was set for T and S and mass conservation was assigned the same weight as the parameter with the highest weight (Tomczak & Large, 1989). In this study, different weights were tested for nutrients, ranging from values 12 to 14 times lower than T, S, and mass conservation. Thereby, T, S, and mass conservation were adjusted to 24 while nutrient weights were fixed to 4 as these weights led to the lowest residuals (Figure S4 in Supporting Information S1).

#### 2.4. Lagrangian Particle Tracking Experiment

Lagrangian Particle Tracking Experiment (LPTE) was conducted to determine the main origin of the water masses crossing the cruise transect and thus to ensure the robustness and reliability of the defined end-member zones (Figure 1b). The Ariane Lagrangian analysis software (<http://www.univ-brest.fr/lpo/ariane>) and a numerical data set from a global ocean circulation model were used to perform this analysis. The data set and LPTE method used in this study are described in the Supporting Information (see Text S1 in Supporting Information S1).

#### 2.5. Statistical Analyses

For [DFe], differences between stations as well as between different depth ranges were tested using a nonparametric Wilcoxon signed-rank test (*wsrt*), due to the nonindependent and non-normally distributed samples. This test was performed using the R function “*wilcox.test*”. Differences were considered significant at  $p < 0.05$ .

Iron anomalies along the transect were obtained by subtracting measured [DFe] during the cruise from theoretical [DFe] deduced from the eOMP. Permutation tests were performed to define a significance level above which the difference obtained actually represents an anomaly. A Monte-Carlo analysis estimated the extent to which DFe anomalies could be affected by analytical errors of both FIA-CL and eOMP, as well as by the variability in end-members [DFe]. Thus, 1,000 permutations of end-member DFe values were performed according to their standard deviation to estimate the propagated errors for each DFe anomaly. Since the highest error was  $\sim 0.2 \text{ nmol kg}^{-1}$ , the anomaly threshold value was set at this value.

### 3. Results

#### 3.1. Dissolved Iron Distribution in the WTSP Ocean

Sections of the DFe distribution are presented in Figure 2, for the cruise transect (a) and for the small transects above the two shallow hydrothermal sources (b and c). Individual DFe vertical profiles are shown in Figure 3 for SD (a, b, c, d, k, and l) and LD (e, f, g, h, i, and j) stations.

##### 3.1.1. South Pacific Gyre: East of the Tonga-Kermadec Arc

The eastern part of the transect includes SD 6, 7, and 8 for which we can observe some differences in the DFe distribution. Stations furthest from the Tonga-Kermadec arc (i.e., SD 7 and 8) were characterized by low [DFe] in the upper layer ( $< 0.2 \text{ nmol kg}^{-1}$ ). Deeper, below 1,000 m, a DFe enrichment was visible ( $0.5\text{--}0.6 \text{ nmol kg}^{-1}$ ) down to 3,000 m for SD 7 and down to 4,000 m for SD 8. The station closest to the arc (i.e., SD 6) was slightly different from the other stations of the gyre. Although [DFe] remain low throughout the whole water column ( $< 0.3\text{--}0.4 \text{ nmol kg}^{-1}$ ) [DFe] were higher than those at SD 7 and 8 (*wsrt*,  $p$ -value: 0.03), particularly in the first 100 m of the water column (*wsrt*,  $p$ -value:  $5.28 \cdot 10^{-6}$ ).

##### 3.1.2. Melanesian Waters: West of the Tonga-Kermadec Arc

Melanesian waters constitute the westernmost part of the transect and include SD 2 and 3. This subregion was characterized by a DFe enrichment in the surface layer compared to the waters of the South Pacific gyre (*wsrt*, 0–200 m,  $p$ -value: 0.02) with [DFe] as high as  $0.4\text{--}0.5 \text{ nmol kg}^{-1}$ . Some peculiarities between the two stations were observable at depth. At SD 2, an increase in [DFe] above  $0.5 \text{ nmol kg}^{-1}$  was visible from 1,000 m to the



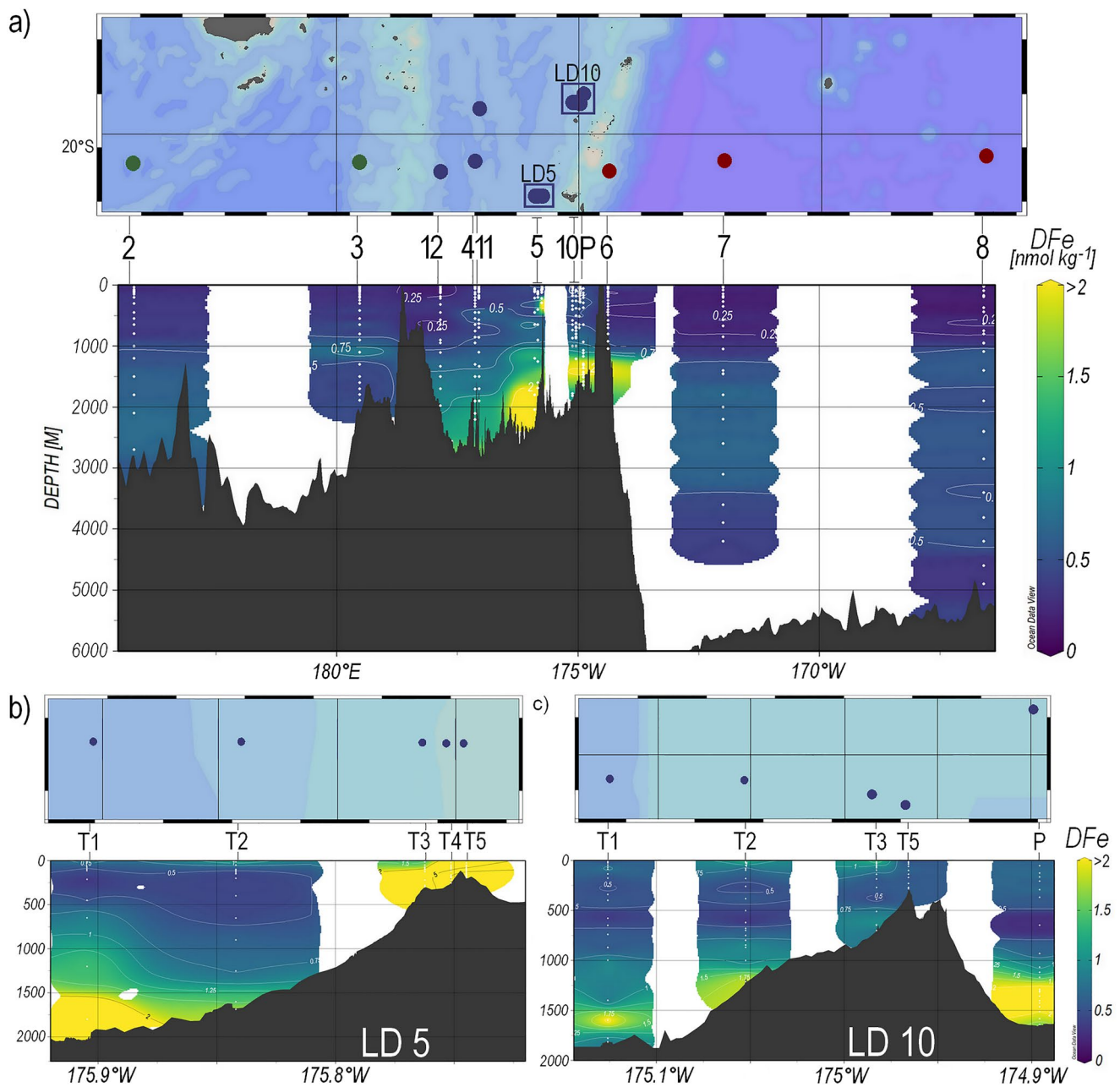


**Figure 2.** Sections of the dissolved iron concentrations ( $\text{nmol kg}^{-1}$ ) along the cruise transect (a) and along two smaller scale transects above long duration (LD) 5 (b) and LD 10 (c). The dots on the maps represent the position of the sampled stations and are colored according to the subregion in which they are located: green for Melanesian waters, blue for the Lau Basin, and red for the South Pacific gyre. Figures were made using Ocean Data View software with weighted-average gridding.

seafloor. An iron peak of  $\sim 0.8 \text{ nmol kg}^{-1}$  centered at the same depth was also observed at SD 3, but  $[\text{DFe}]$  decreased rapidly below this depth, becoming constant at  $\sim 0.4 \text{ nmol kg}^{-1}$  from 1,200 m to the seafloor.

### 3.1.3. Lau Basin

**SD stations.** The Lau Basin, located between the Lau and Tonga ridges, is the central part of the transect and includes SD 4, 11, and 12 as well as LD 5 and 10 where two shallow hydrothermal sources were studied. In this oceanic basin, higher  $[\text{DFe}]$  were observed than in the South Pacific gyre (*wstr*, *p*-value: 0.003) as well as in Melanesian waters (*wstr*, *p*-value: 0.04) for all stations and over the entire water column. As for the other stations in the transect, some local differences were depicted for each profile. The westernmost station of the Lau Basin (i.e., SD 4) was characterized by  $[\text{DFe}]$  of 0.3–0.4  $\text{nmol kg}^{-1}$  between 0 and 800 m. Below 800 m, an enrichment

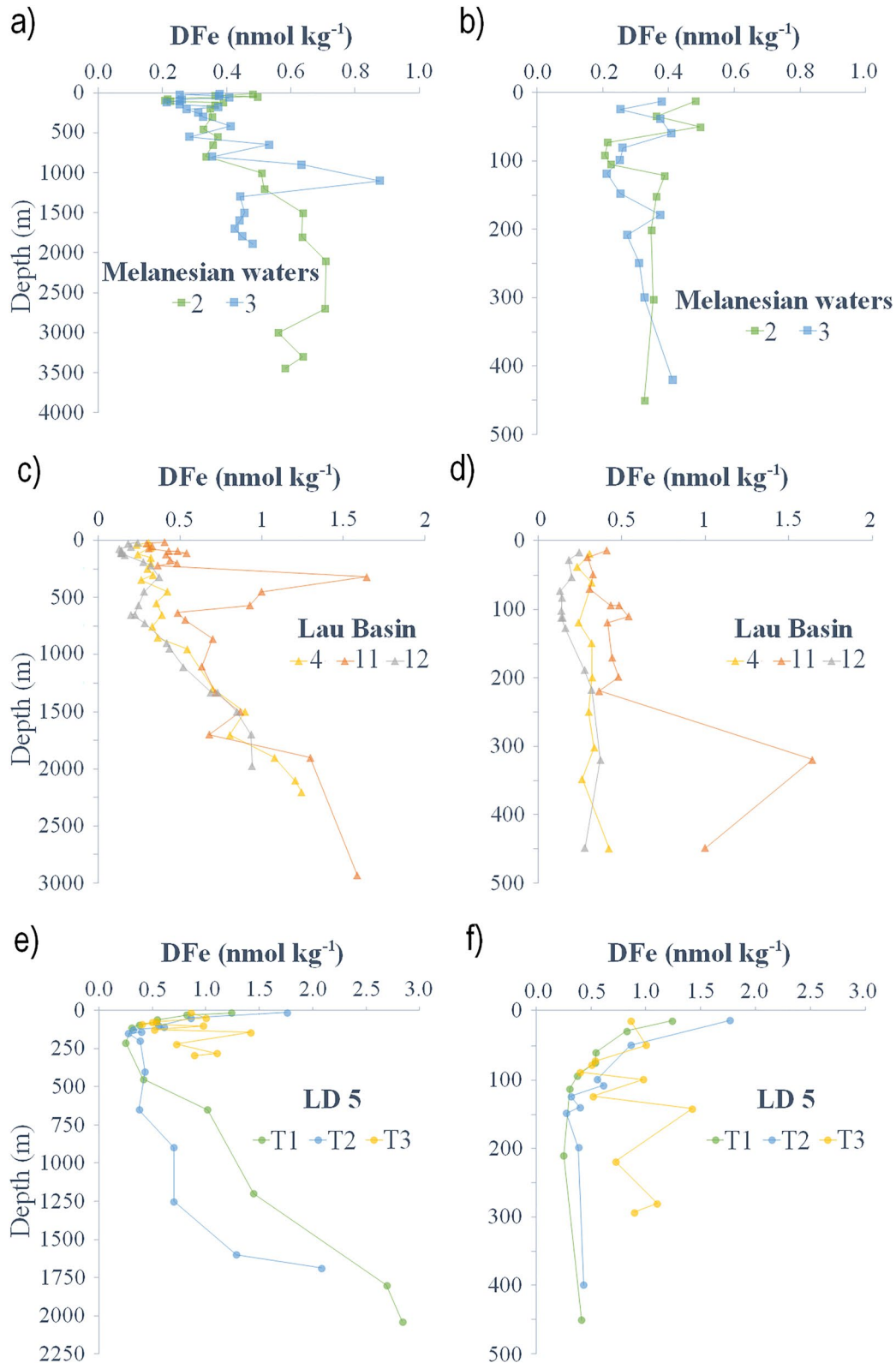


**Figure 3.** Dissolved iron (DFe) profiles in Melanesian waters (a) and (b), Lau Basin (c) and (d), in the different substations T5 to T1 of LD 5 (e–h), LD 10 along with Proxnov (i and j) and South Pacific gyre (k and l). DFe distribution at LD 5–T5 (i.e., the cast above the hydrothermal source) and LD 5–T4 are plotted separately (g) and (h) due to the high (DFe). Each of the profiles from each region was plotted over the entire water column (a, c, e, g, i, and k) and then over 0–500 m (b, d, f, j, and l) or 0–100 m (h). Note the different axis scales.

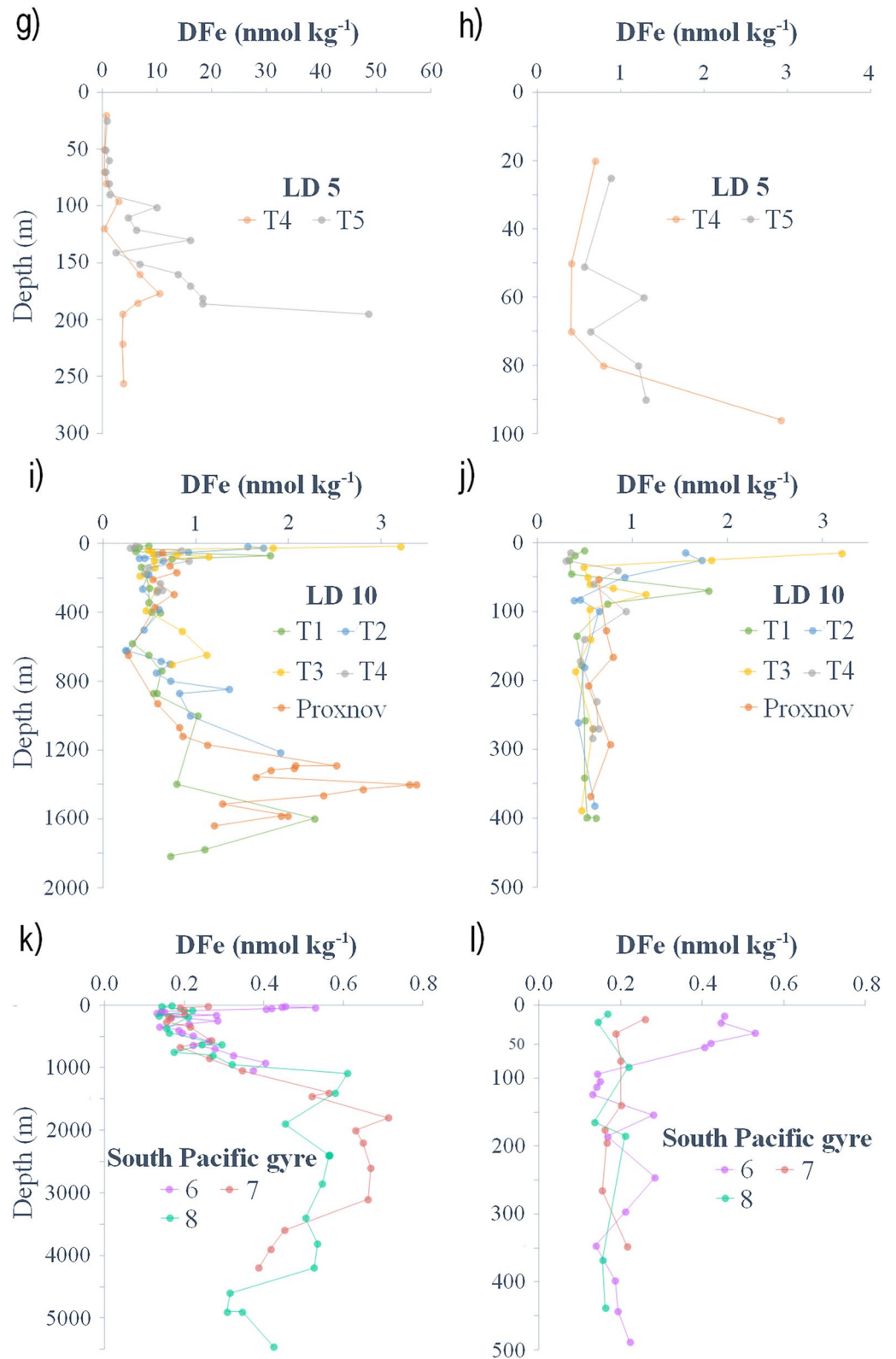


Figure 3. (Continued)

was observed with a maximum [DFe] of  $1.2 \text{ nmol kg}^{-1}$  at  $\sim 2,200 \text{ m}$ . SD 12 presented the least enriched surface layer, with [DFe] similar to those observed to the east ( $\sim 0.2 \text{ nmol kg}^{-1}$ , *wstr*, *p*-value: 0.54). At depth, a gradual increase of [DFe] to  $\sim 1 \text{ nmol kg}^{-1}$  was observed from 600 m to the seafloor. SD 11 had the highest [DFe] of the SD in the Lau Basin. In the surface layer, high [DFe] were observed ( $0.4\text{--}0.6 \text{ nmol kg}^{-1}$ ). As for SD 12, a gradual increase of [DFe] up to  $1.6 \text{ nmol kg}^{-1}$  was observed at SD 11 from 600 m to the seafloor. For both stations, a peak centered at  $\sim 320 \text{ m}$  was visible, relatively low for SD 12 ( $0.4 \text{ nmol kg}^{-1}$ ) and rather high for SD 11 ( $1.6 \text{ nmol kg}^{-1}$ ).

**LD 5.** At LD 5, five substations were investigated: T5, located where the highest acoustic and chemical anomalies were found, and T4, T3, T2, and T1, which were located at 0.6, 2, 10, and 17 km from T5, respectively (Figures 2b and 3d, 3e). At T5, a high [DFe] ( $\sim 50 \text{ nmol kg}^{-1}$ ) was observed 5 m above the seafloor (195 m), decreasing rapidly to  $\sim 18 \text{ nmol kg}^{-1}$  at 185 m. These high [DFe] were maintained around  $10\text{--}18 \text{ nmol kg}^{-1}$  up to 100 m before decreasing to a [DFe] of  $\sim 1 \text{ nmol kg}^{-1}$ . At T4 [DFe] were high in the surface layer, ranging from 0.4 to  $2.9 \text{ nmol kg}^{-1}$  and even higher at depth ( $\sim 4\text{--}6 \text{ nmol kg}^{-1}$ ). Two [DFe] peaks were observed at 100 and 175 m. Fluctuating profiles were observable at T3 from surface to bottom, with [DFe] varying between 0.4 and  $1.4 \text{ nmol kg}^{-1}$  and high [DFe] were visible just at the surface ( $0.8\text{--}1 \text{ nmol kg}^{-1}$  at 0–50 m). The profiles of T1 and T2 were quite similar, characterized by high [DFe] in the first 100 m of the water column ( $0.5\text{--}2 \text{ nmol kg}^{-1}$ ) [DFe] remained constant at  $\sim 0.5 \text{ nmol kg}^{-1}$  between 200 and 600 m before gradually increasing to the seafloor ( $2\text{--}2.5 \text{ nmol kg}^{-1}$ ).

**LD 10.** As for LD 5, four substations were surveyed at LD 10: T5, which was located on the edge of a small caldera summit, and T3, T2, and T1, which were 2, 8, and 15 km from T5. At T5, high [DFe] were observed in the entire profile (average  $\sim 0.6 \text{ nmol kg}^{-1}$ ). However, DFe enrichment was not as high as the one observed at LD 5-T5 (*wstr*, *p*-value: 0.01). At T3, surface [DFe] were higher than just above the caldera summit, ranging from 2 to  $3 \text{ nmol kg}^{-1}$  between 0 and 35 m. Below 35 m, the profile remained constant at  $\sim 0.5 \text{ nmol kg}^{-1}$ . At T2 [DFe] were still high between 0 and 80 m ( $0.5\text{--}1.5 \text{ nmol kg}^{-1}$ ). Below 80 m and down to 200 m [DFe] decreased from 0.5 to  $0.2 \text{ nmol kg}^{-1}$ , followed by an increase to  $\sim 2 \text{ nmol kg}^{-1}$  from 200 m to the seafloor. At T1 [DFe] were stable along the entire profile ( $\sim 0.5 \text{ nmol kg}^{-1}$ ) except for two  $\sim 2 \text{ nmol kg}^{-1}$  peaks observed at 100 and 1,000 m. At Proxnov [DFe] of  $\sim 0.7 \text{ nmol kg}^{-1}$  were observable throughout the water column with maxima below 1,000 m ( $2.5, 3.5,$  and  $2 \text{ nmol kg}^{-1}$  at 1,250, 1,400, and 1,600 m, respectively).

## 3.2. Water Mass Structure in the WTSP Ocean

### 3.2.1. Water Mass Definition

In this section, the different water masses were characterized based on Talley et al. (2011) and Tomczak and Godfrey (2003). Properties of each end-member are presented in Table 1.

The lower surface layer (100–200 m) is characterized by seasonal changes in water mass properties due to ocean-atmosphere exchanges that have a significant impact on the temperature and salinity of the water mass (e.g., seasonal temperature variability, subtropical evaporation, and equatorial excess precipitation). This analytical issue was circumvented by creating the ASW, which is the only end-member contributing significantly to this layer. The main thermocline (200–700 m) includes the Subtropical Underwater (STUW) and the Western South Pacific Central Water (WSPCW). STUW originates from the subduction of high salinity waters from the equatorial part of the subtropical gyre and is associated with a shallow salinity maximum. Created by subduction and diapycnal mixing, WSPCW exhibits a linear temperature-salinity relationship over a wide range down to the intermediate layer. The intermediate layer (700–1,300 m) was composed solely of AAIW, a low-salinity water mass originating from the sea surface at sub-Antarctic latitudes and characterized by a salinity minimum reached at 700 m. AAIW circulates around the subtropical gyre from the Southeastern Pacific, extending northwestward as tongues of low-salinity, high-oxygen water, and enters the tropics in the Western Pacific. The deep layer ( $>1,300 \text{ m}$ ) contains the Pacific Deep Water (PDW) and the Lower Circumpolar Deep Water (LCDW). PDW originates from the equatorial Pacific and flows southward. It is formed in the Pacific interior from the upwelling of the Antarctic Bottom Water. PDW is the oldest water in the global ocean, characterized by low oxygen, high nitrate, and well-mixed temperature and salinity. LCDW originates from the Southern Ocean and overlaps the depth and density ranges of PDW. It can, however, be distinguished from PDW by a maximum of salinity and

oxygen and a nitrate minimum. The property-property profiles of the data set used for the eOMP and the properties of the defined end-members are shown in Figure S5 in Supporting Information S1.

*A posteriori*, LPTE analyses were performed to ensure that the area chosen for the position and depth of each end-member agreed with the particle trajectories modeled in the region. The results of these analyses are shown in Figures S6, S7, and S8 in Supporting Information S1. These analyses support the contribution of STUW to the thermocline layer of the cruise transect with particles following the South Pacific gyre circulation between 200 and 400 m, reaching the selected area for this water mass. Trajectories are also in good agreement with the zone defined for WSPCW as particles, originating from the Southern Ocean, crossing the Tasman Sea between 200 and 400 m before reaching the area of the cruise transect. LPTE trajectories were consistent with the current understanding of AAIW circulation: AAIW enters the Pacific Ocean from Eastern New Zealand between 700 and 1,500 m and flows to the WTSP via several pathways extending from the subtropical gyre, originating mainly from the Southeastern Pacific. The particle trajectories were also in agreement for PDW, as particles from the equatorial Pacific reach the PDW-defined zone at 1,500–2,500 m and flow toward the transect. Regarding LCDW, the LPTE analysis was consistent with the end-member area chosen for the eastern part of the transect, as particles from the Southern Ocean flow east of New Zealand before heading northwest and reaching the area of the transect. This analysis also corroborates the lack of LCDW contribution to the western part of the transect as demonstrated by the eOMP (see Section 3.2.2) since no particles originating from this water mass reach the western part of the transect.

### 3.2.2. Vertical Contribution of Water Masses Along the Cruise Transect

The eOMP results allowed a detailed description of the contribution and distribution of the selected water masses (i.e., end-members) along the cruise transect (Figure 4). A uniform zonal distribution of water masses was visible along the cruise transect, with the exception of the two deep end-members, PDW and LCDW, for which a different distribution for the eastern and western parts of the transect was observed. While PDW and LCDW contributed almost equally to the water masses in the eastern part of the transect below 1,000 m, PDW was dominant in the western part (up to 90%). LCDW thus contributes to only 10%–30% of the water masses in the western part of the transect, which contrasts with its high contribution (up to 100%) in the deepest waters of the South Pacific gyre.

According to the eOMP, the lower surface layer was mainly occupied by ASW with contributions greater than 60%–90% in the 100–200 m depth range. This contribution decreased rapidly with depth to less than 30% at ~250 m and reached zero contribution below 750 m. The thermocline layer was dominated by two water masses: STUW and WSPCW. STUW was present at depths between 100 and 450 m and reached its maximum contribution (>40%) between 150 and 300 m. Below STUW, a layer of WSPCW was present along the transect with contributions exceeding 60% between 250 and 500 m. The maximum contribution of WSPCW was at ~400 m (60%–70%). AAIW was present over a depth range of 450–1,300 m and strongly dominated the intermediate layer with a contribution exceeding 90% between 700 and 1,000 m. Its contribution decreased rapidly from 80% at 1,000 m to 40% at 1,300 m. The deep layer was occupied by two water masses that displayed differences in contribution for the western and eastern parts of the transect. Mixed with AAIW between 1,000 and 1,300 m, PDW occupied both intermediate and deep layers. It dominated the portion between 1,300 and 2,500 m with a contribution ranging from 60% to almost 100% in the eastern part of the transect. Its maximum contribution (60%–90%) occupied a larger depth range in the western part as it reached the seafloor of the Melanesian waters (~3,000 m) and Lau Basin (~4,000 m). In contrast, the deeper seafloor of the South Pacific gyre (~6,000 m) was not reached by PDW but by LCDW, a water mass present throughout the eastern section from 2,000 m to the seafloor. Initially mixed with PDW until 3,150 m (40%), its contribution increased to 60%–70% between 3,200 and 4,000 m. LCDW then strongly dominated the deep layer below 4,000 m with a contribution ranging from 90% to 100%. However, in the western part of the transect, LCDW was only present between 2,500 m and the seafloor (~3,000 m) in Melanesian waters and its contribution did not exceed 25%. Its contribution in the Lau Basin was negligible.

### 3.3. Iron Anomalies Along the WTSP Ocean

The eOMP-derived DFe transect represents the iron distribution resulting solely from water mass transport and physical mixing and acts as a control section without local sources. Those theoretical [DFe] were very low and

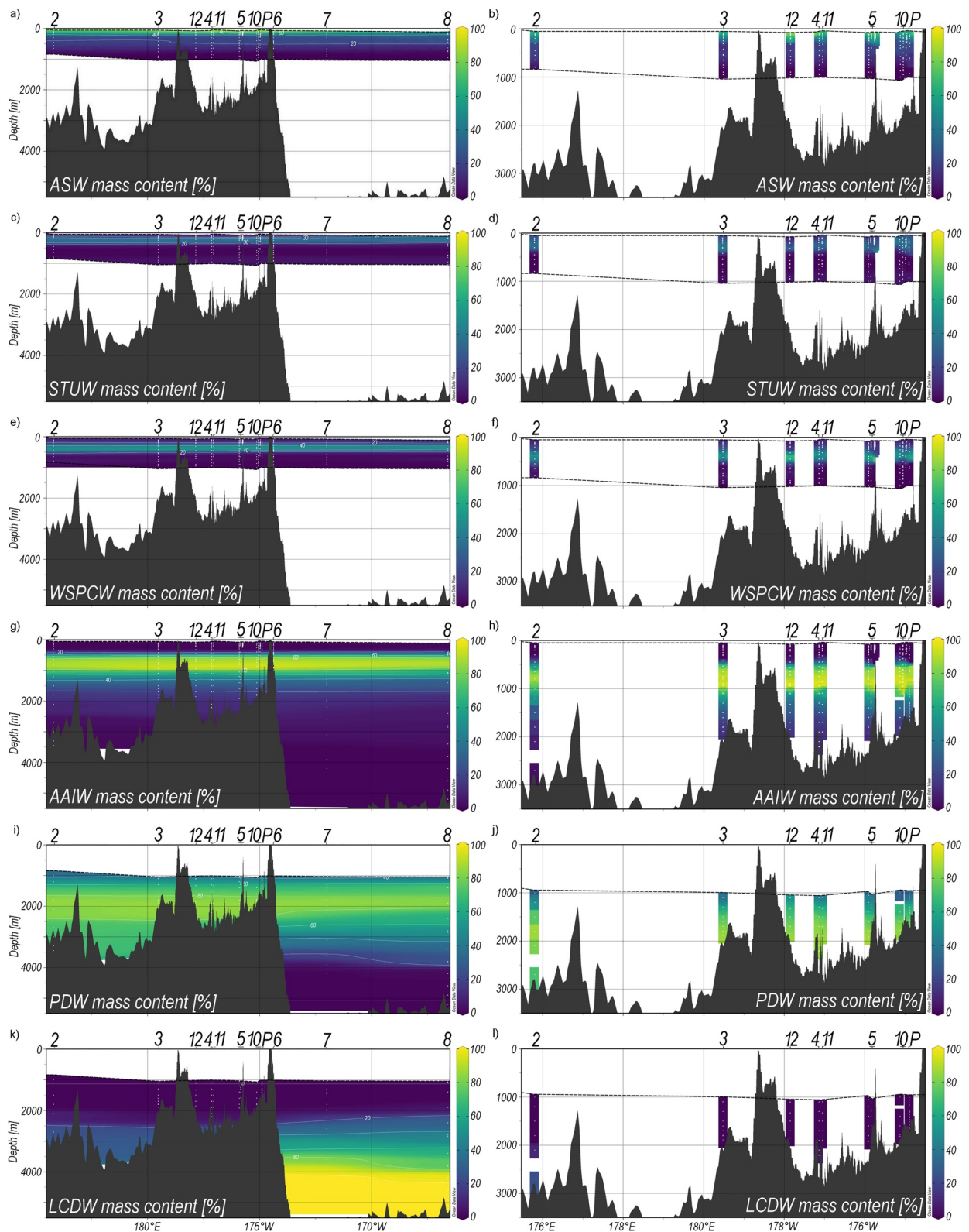


Figure 4.

homogeneous across the transect (Figure 5a) depicting classic oceanic iron profiles for each station: low [DFe] in the upper layer (0.2–0.3 nmol kg<sup>-1</sup>) and slightly higher [DFe] at depth (>0.4 nmol kg<sup>-1</sup>).

Iron anomalies presented in Figure 5b were obtained by subtracting measured [DFe] (Figure 2a) from theoretical [DFe]. The lowest anomalies (~0.09 nmol kg<sup>-1</sup>) below the threshold value were observed for SD 6, 7, and 8. In the Melanesian waters, anomalies were higher but still below the threshold value, except for a few significant anomalies of ~0.3 nmol kg<sup>-1</sup> observed at 1,000 m for SD 3. Significant and large anomalies were found for stations located in the Lau Basin both at surface and at depth, except for SD 4 and 12 for which anomalies were only present below 1,500 m.

DFe stocks attributed to local sources (“anomaly stocks”) integrated over different layers are shown in Figure 5c. No significant differences in anomaly stocks were observed between the three depth layers (100–200 m, 200–1,000 m, and 1,000 m–bottom) for stations located east of the Tonga-Kermadec arc (SD 6, 7, and 8) and in Melanesian waters (SD 2 and 3). In contrast, some differences were observed in the Lau Basin depending on the depth layer considered, except for the westernmost SD 12. Large anomaly stocks were observable in all three layers at SD 12 (up to 0.4 μmol m<sup>-2</sup>) but only in the deep layer for SD 4 (0.3 μmol m<sup>-2</sup>). At LD 5, high anomaly stocks were visible in the lower surface layer from T5 to T3 (from 12.4 to 0.8 μmol m<sup>-2</sup>) but decreased at T2 (0.17 μmol m<sup>-2</sup>). In contrast, anomaly stocks in the deep and intermediate layers remained high for all LD 5 substations (0.4–3.6 μmol m<sup>-2</sup>). At LD 10, large anomaly stocks were visible in the lower surface layer at all substations although they were 10 times lower than at LD 5. At Proxnov, a large anomaly stock was visible in the lower surface and deep layers (0.5 and 1.1 μmol m<sup>-2</sup>, respectively).

## 4. Discussion

### 4.1. Physical Circulation in the Study Region

Physical processes at play in the region may provide insight into the distribution and fate of DFe. The large-scale surface circulation of the WTSP Ocean is well characterized (Reid, 1997) and is dominated by the anticyclonic South Pacific gyre. The South Equatorial Current (SEC) flows westward through the equatorial band and splits into several branches when it reaches the Lau Basin due to blocking of the SEC by islands associated with the Tonga and Lau arcs (Webb, 2000). In the western boundary, the SEC splits and joins the East Australian Current that runs along the northwest coast of Australia before flowing eastward to feed the southern branch of the gyre. It then joins the Humboldt Current that flows northward along the continental coast of South America (Tomczak & Godfrey, 2003). Gyre waters then return to the equator through the SEC (Ganachaud et al., 2014). Thus, large-scale surface circulation patterns of the study area illustrate the presence of predominant westward currents associated with the SEC.

The eOMP coupled with a LPTE performed for this study allowed assessing the structure and mixing of water masses in the WTSP Ocean and estimating the theoretical distribution of DFe at the scale of our transect. As most geographic variation in water properties occurs in the meridional direction in the Pacific Ocean (Talley et al., 2007), it is not surprising that results showed a quasi-uniform zonal distribution of water masses in the transect conducted sufficiently far from the East Australian Current along 20°S. Due to bathymetry sills, deep water masses are not present in the Lau Basin, as its bowl-shaped seafloor prevents their entry. Thus, the westward-flowing subtropical gyre appears to collide with the bathymetric barrier represented by the Tonga-Kermadec arc, which would affect the way hydrothermal inputs spread downstream within the Lau Basin.

This regional circulation can be discerned by the trajectories of different autonomous instruments deployed during the cruise: SVP drifters at surface (0–15 m, Figure S9 in Supporting Information S1), profiling floats at depth (1,000–1,500 m; Figure S10 in Supporting Information S1), and a free-drifting mooring line (over the 0–1,000 m layer; Figure 6b). Along the Tonga-Kermadec arc, the 5-day mooring line trajectory showed a main

**Figure 4.** Contributions (%) of the different water masses to the cruise transect at each sampling depth according to the extended optimum multiparameter analysis (eOMP) for (a) the Artfactual Surface Water (ASW), (c) the Subtropical Underwater (STUW), (e) the Western South Pacific Central Water (WSPCW), (g) the Antarctic Intermediate Water (AAIW), (i) the Pacific Deep Water (PDW), and (j) the Lower Circumpolar Deep Water (LCDW). The right panels represent the contributions of each water mass in the western part of the transect that includes Melanesian waters short duration (SD) 2 and 3) and Lau Basin (SD 4, 11, and 12; long duration 5 and 10) with (b) ASW, (d) STUW, (f) WSPCW, (h) AAIW (j) Pacific Deep Water, and (l) LCDW. Sampling points are represented by white dots. The black dotted line represents the boundary above which the eOMP could not be applied (i.e., due to non-conservative parameters in the upper surface layer and residuals >5%). Figures were made using Ocean Data View software with weighted-average gridding (left panels) and quick gridding (right panels).

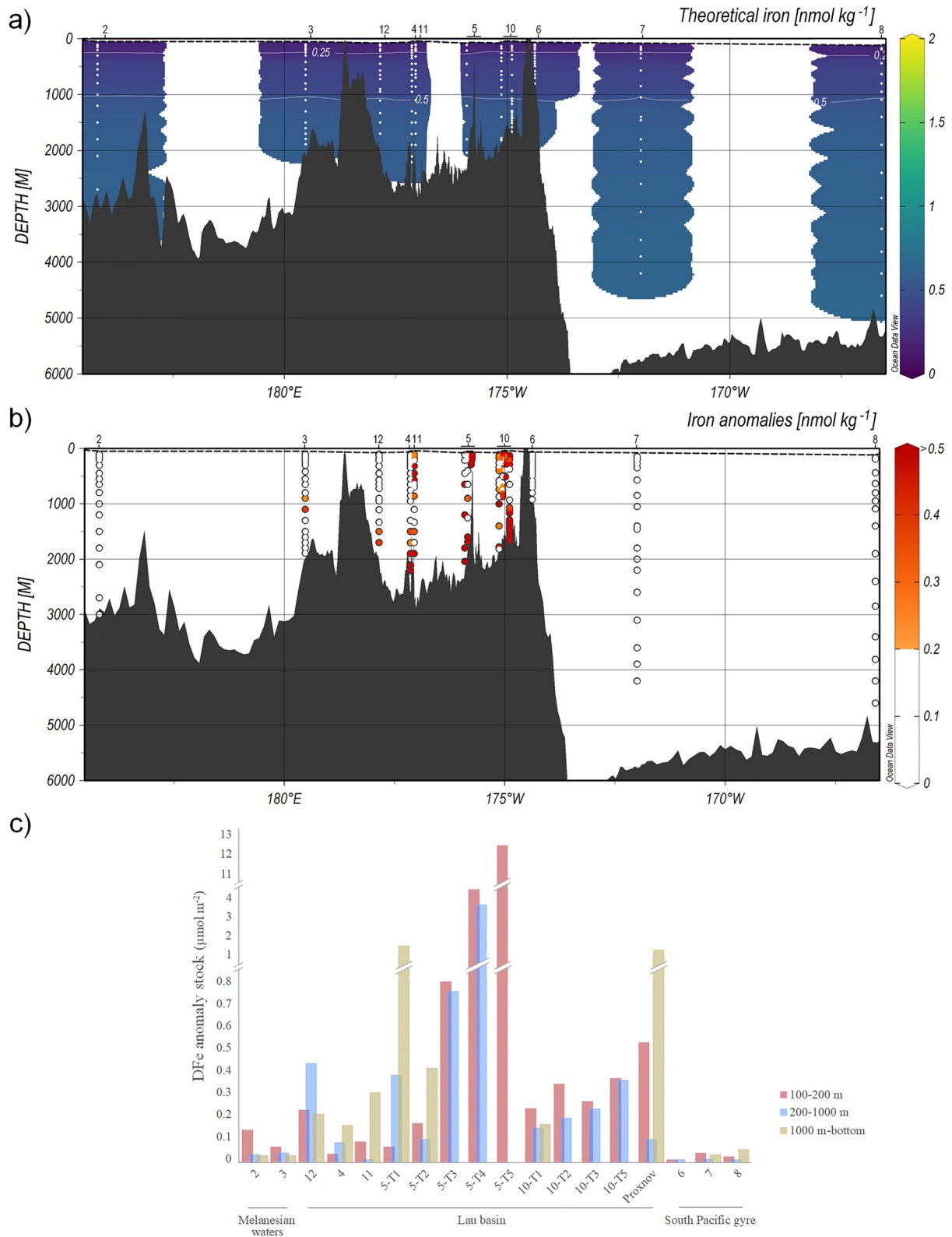


Figure 5.



stream heading southwest, in agreement with profiling floats trajectories before veering west in the center of the Lau Basin. In comparison, SVP drifter trajectories showed enhanced relative dispersion and five times larger velocities, indicating that in the surface layer, turbulent flow prevails over the mean southwestern circulation. Residence times in the Lau Basin were about a few weeks for drifters at surface (Figure S9 in Supporting Information S1) and several months for profiling floats at 1,000–1,500 m (Figure S10 in Supporting Information S1). It should be noted that such a description remains qualitative given the sparsity of the data set, however, in agreement with basin-scale estimates reported in the literature (Davis, 2005; Zhurbas & Oh, 2004). This is also in agreement with Rousselet et al. (2018) that reported enhanced eddy activity in the surface layer west of 170°W.

## 4.2. Dissolved Iron Distribution in the WTSP Ocean

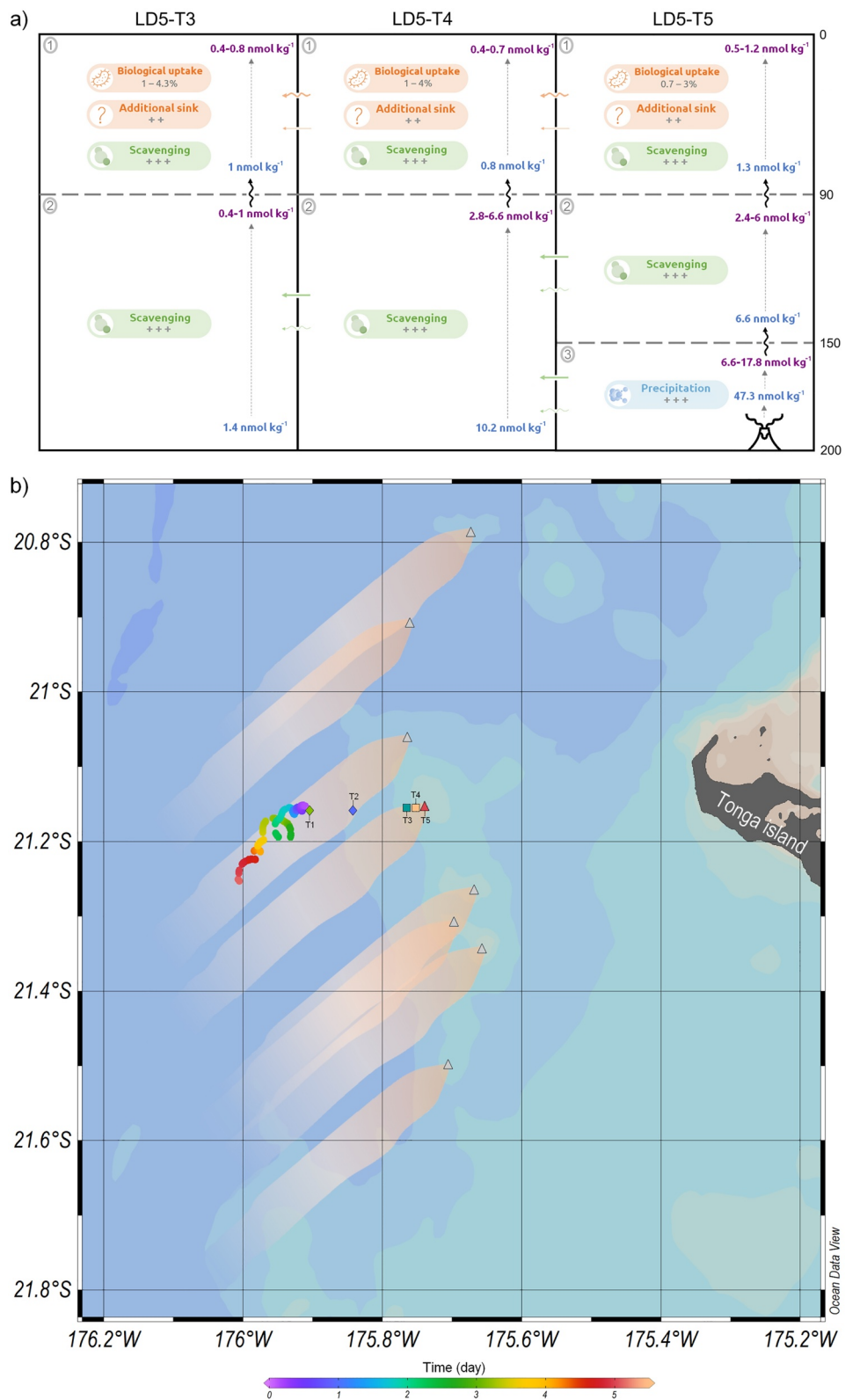
This study provides new insights into the oceanic iron cycle for several reasons. The Pacific Ocean is severely undersampled, especially for trace metals such as iron (Bruland & Lohan, 2006) and in the WTSP region for which very few data are available (Baumberger et al., 2014, 2020; Campbell et al., 2005; Cohen et al., 2021; Fitzsimmons et al., 2014; German et al., 2006; Guieu et al., 2018; Lupton et al., 2012; Massoth et al., 2007). It yet represents a key region for understanding global DFe dynamics, particularly related to diazotroph activity (Bonnet et al., 2017). Furthermore, deep hydrothermal iron inputs are widely studied in all ocean regions in contrast to those induced by shallow hydrothermal vents associated with island arcs (Hawkes et al., 2014). The Tonga-Kermadec arc hosts a high density of submarine volcanoes associated with shallow hydrothermal sites (~2.6 vents/100 km; German et al., 2016). In the region, Guieu et al. (2018) measured elevated [DFe] in the photic layer (0–150 m) and attributed them to shallow hydrothermal vents. Such shallow systems releasing DFe-rich plumes have also been observed along the Mariana arc (up to 75 nM; Buck et al., 2018; Resing et al., 2009). Here, for the first time, a dedicated survey of the fate of hydrothermal iron inputs from shallow sources has been conducted.

### 4.2.1. Iron Sources: Origin of the Dissolved Iron Inputs

Our results demonstrated that physical dynamics have a low impact on the DFe distribution along the transect. DFe distribution inferred from the eOMP shows low theoretical [DFe] present throughout the transect including in the Lau Basin. These theoretical [DFe], similar to open ocean iron distribution (Blain et al., 2008; Johnson et al., 1997), allowed us to conclude that DFe originates, almost certainly, from local sources present in the WTSP region.

In the eastern part of the transect, the absence of DFe anomalies demonstrated that no local sources provide iron in the waters of the South Pacific gyre. However, it should be noted that a DFe enrichment of  $\sim 0.57$  nmol kg<sup>-1</sup> was measured between 1,000 and 3,000 m in the gyre (Figure 2a; SD 7 and 8). It was initially considered as a deep distal plume from the East Pacific Rise (EPR), as Resing et al. (2015) measured a plume rich in DFe ( $\sim 0.75$  nmol kg<sup>-1</sup> at 152°W) thousands of km away from the source (located at 113°W). Although this was a more northerly source, the EPR extends from North America to the tip of South America and hosts numerous vents that could have a similar impact on the entire ocean basin (Hudson et al., 1986; Menard, 1960). However, this hypothesis has been refuted by the eOMP, which demonstrated the absence of DFe anomalies (above the 0.2 nmol kg<sup>-1</sup> threshold, see Section 2.5) to the east, although hydrothermal <sup>3</sup>He enrichment from the EPR ( $\sim 30\%$ ) was measured at  $\sim 2,500$  m at 10–12°S, 160–170°W by Lupton et al. (2004). This suggests that the anomalies measured by Resing et al. (2015) ultimately merge with the [DFe] of the native deep water mass ( $0.61 \pm 0.07$  nmol kg<sup>-1</sup>) and are no longer distinguished on this larger scale ( $\sim 6,000$  km from the EPR) with this significance threshold. An absence of anomalies was also observed in Melanesian waters, except for two anomalies visible at 1,000 m at SD 3, suggesting the absence of local sources in this subregion. It has to be noted that the iron-rich plume centered at  $\sim 180^\circ$ E identified by Guieu et al. (2018) at the western border of the Lau arc in March 2015 was not observed during our cruise. As hypothesized by the authors, the high [DFe] measured during this cruise could have been linked to a short-duration event-plume related to an important submarine eruption event. The most notable DFe

**Figure 5.** (a) Theoretical dissolved iron (DFe) concentrations along the cruise transect obtained from the extended optimum multiparameter analysis. This figure was made using Ocean Data View software with weighted-average gridding. (b) Iron anomaly representing the difference between measured and theoretical DFe concentrations. White dots correspond to iron anomaly values below the 0.2 nmol kg<sup>-1</sup> significance threshold. (c) Histograms of the DFe anomaly stocks across the region integrated over the lower surface (100–200 m, red), intermediate (200–1,000 m, blue), and deep layers (>1,000 m, brown). The order of appearance of the stations on the histogram is organized according to the longitudinal distribution of the subregions studied: the Melanesian waters (i.e., SD 2 and 3), the Lau Basin (i.e., SD 4, 11, and 12) also including LD 5 and 10, and finally the South Pacific gyre (i.e., SD 6, 7, and 8).



anomalies were found in the Lau Basin, particularly near the Tonga-Kermadec arc, where hydrothermal sources have already been reported (de Ronde et al., 2001; Massoth et al., 2007). Strong anomalies were visible both at surface and at depth, suggesting the presence of one or more local iron sources along this arc system.

As described previously, multiple iron sources exist in the open ocean. Atmospheric iron inputs can be dismissed, as they were quantified by Guieu et al. (2018) as being at the lower end of reported values for the remote ocean and could not explain the large increase observed with depth. In the WTSP region, four sources can potentially influence the distribution of DFe. Remineralization can impact the DFe distribution depending on the nature of the particulate iron (PFe) present (Boyd et al., 2010; Bressac et al., 2019). This region is both a productive zone, rich in biogenic particles favoring remineralization, and a volcanic zone, rich in lithogenic particles enhancing scavenging. A balance between the two (i.e., source vs. sink) could prevail in the region. However, remineralization has been quantified as redissolving only 1%–2% of PFe (Boyd et al., 2010). In addition, Abadie et al. (2017) showed through an iron isotope study that remineralization occurs preferentially in intermediate waters, with particle desorption (John & Adkins, 2012; Labatut, 2014) being the primary source of DFe in deep waters. Thus, remineralization could not explain the DFe anomalies measured both at surface and at depth in the Lau Basin. Iron inputs of island origin could have a possible impact near the Melanesian archipelagos. This region hosts many ferromagnesian islands that could supply terrigenous nutrients, including iron, as hypothesized by Shiozaki et al. (2014), although these fluxes have not yet been quantified. Similarly, simulations from Dutheil et al. (2018) in the region showed that sediment-associated iron inputs near island margins could partly control *Trichodesmium* development. However, the latter two sources would primarily affect the coastal distribution of DFe at the WTSP Ocean scale and could not explain the observed patterns away from the islands. Model estimates (Tagliabue et al., 2010) and in situ measurements (Fitzsimmons et al., 2014, 2017; Resing et al., 2015) have shown a large-scale impact of deep hydrothermal-derived plumes on the DFe distribution, up to more than 4,000 km off-axis. Such inputs could fertilize the entire Lau Basin and may explain the DFe anomaly patterns observed in this study. In this context, other sources seem negligible at the scale of the observed DFe enrichment, especially since it is remote from the islands.

Consistent with this hypothesis, literature and cruise data provide evidence for the hydrothermal origin of DFe in the WTSP Ocean for several reasons. This region has been reported to host numerous submarine volcanoes associated with a high density of hydrothermal fields (de Ronde et al., 2001; Massoth et al., 2007), and of these, two shallow hydrothermal sources were studied extensively during the cruise. LD 5-T5 appears to be the most active hydrothermal site. Chemical and acoustic features, typical of hydrothermal plumes (Dick et al., 2013; Resing et al., 2009; Santana-Casiano et al., 2013), were measured at this site during the cruise (see Bonnet et al. (under review) and Figure S11 in Supporting Information S1), including a suboxic environment with low O<sub>2</sub> concentrations (down to 150 μM), low pH (down to 6.5), high levels of CH<sub>4</sub> (up to 104 nM), CO<sub>2</sub> (up to 645 μM), and H<sub>2</sub>S (Portlock, pers. comm. 2022). As reported in the literature in this area (Massoth et al., 2007) and elsewhere (e.g., Dick et al., 2013; González-Vega et al., 2020; Tarasov, 2006), significant amounts of DFe were released by this hydrothermal site, especially since concentrations up to 50 nmol kg<sup>-1</sup> were measured at 5 m above the seafloor. In addition, the highest DFe anomaly stock was recorded in the lower surface layer (100–200 m) at this site and was 500 times higher than in the South Pacific gyre. Comparatively, LD 10-T5 seems to be a less active site, with a DFe anomaly stock in the lower surface layer 35 times smaller than LD 5-T5 but still 15 times higher than in the gyre. Multiple clear acoustic anomalies were observed in the multibeam survey over this hydrothermal site during the cruise, indicating the presence of many weakly active sources. However, it should be noted that the DFe anomalies recorded at this site could also originate from the recent submarine eruption of New Late'iki one month before the cruise (i.e., 13–23 October, 2019; Plank et al., 2020). This assumption seems reasonable since the New Late'iki eruption site, Proxnov, and LD 10-T5 were only 10 and 15 km apart, respectively, and high DFe anomaly stocks were measured in the lower surface layer at Proxnov. A large anomaly stock was also estimated

**Figure 6.** (a) Representation of the budget for substations T5, T4, and T3 of long duration (LD) 5. The gray circled numbers at each substation correspond to the number of the sub-boxes representing the (a) upper photic, (b) lower photic, and (c) suboxic layers. The depths at the right correspond to the limit of each sub-box. The dissolved iron concentration ([DFe]) at the greater depth of each sub-box is in blue. The range of [DFe] (i.e., min-max) within each sub-box is in purple. The intensity of each process is illustrated by “+ +” for moderate DFe sink and “+ + +” for strong sink. Orange cells represent processes acting exclusively in the upper photic layer, blue cells represent precipitation acting mainly in the suboxic layer while green cells represent processes that act in all layers. Wavy arrows represent diffusive fluxes (vertical or horizontal) and straight arrows represent advective transports. (b) Cartoon illustrating the dispersion of the measured plume in the Lau Basin at substations T5, T4, and T3 of LD 5 and the illustration of the possible many plumes from sources further north or south of our Tonga arc study area. The colored points represent the 5-day southwestward trajectory of the free-drifting mooring line (vertical integration of the currents in the 0–1,000 m layer) deployed at LD 5-T1. Note that the plume spreading was drawn according to that trajectory.

in the deep layer for this substation. Similarly, very abundant volcanic material was collected at 1,000 m in sediment traps deployed at LD 10-T1 (Leblanc, pers. com. 2021) associated with the presence of a deep horizon of turbidity-identified particles. It can therefore be hypothesized that these large DFe anomalies and high particle abundance originate at least partly from this submarine eruption.

The strong DFe anomalies observed near the Tonga-Kermadec arc are thus not limited to the lower surface layer. Indeed, anomalies of the same order of magnitude have also been measured in the deep layer below 1,000 m at LD 5-T1 and T2. This suggests the presence of many additional deep sources along the Tonga-Kermadec arc as reported in the literature (de Ronde et al., 2001; Massoth et al., 2007), some of them probably located near LD 5-T1 where the highest anomaly stock was measured at depth. Such deep sources are known to release DFe-rich fluids, sometimes a million times enriched relative to ambient concentrations in the deep ocean (Von Damm, 1990) and the emitted plumes can be transported far from the source (Fitzsimmons et al., 2014, 2017; Resing et al., 2015).

#### 4.2.2. Iron Sinks: Distribution and Fate of Dissolved Iron

The question of the fate of DFe (i.e., stabilization vs. loss) originating from deep and shallow hydrothermalism is also of great importance, particularly due to its influence on the biological carbon pump. Hydrothermal DFe was long thought to be lost near the source, but recent studies have shown that hydrothermal DFe from deep ocean ridges can be transported thousands of kilometers from the source (Fitzsimmons et al., 2014, 2017; Resing et al., 2015; Wu et al., 2011).

In agreement with these previous studies, our data show a wide dispersion of deep hydrothermal DFe over several hundred kilometers (~300 km). As mentioned in Section 4.2.1, deep sources appear to be active in the vicinity of the Tonga arc, around 1,000 m near LD 5-T1. Thus, anomalies measured further west may be associated with the westward dispersion (see Section 4.1) of deep plumes originating from the Tonga arc. This deep iron-rich plume can be traced hundreds of kilometers from the source in the Lau Basin. However, the significant anomalies estimated in Melanesian waters (SD 3, ~1,000 m) could also originate from the Lau arc. Further investigations are needed to better interpret those anomalies far from the Tonga arc. The presence of such high concentrations far from the arc where hydrothermal sources have been identified (de Ronde et al., 2001; Massoth et al., 2007; Stoffers et al., 2006) is due to both advective transport and in situ geochemical conditions that allow DFe to remain in solution. The presence of strong iron-binding ligands may explain the stabilization of DFe at depth, especially since ligands have been reported to be abundant in hydrothermal plumes (Bennett et al., 2008; Sander & Koschinsky, 2011). Iron-ligand complexes (Fe-L) are known to enhance the solubility and stabilization of DFe (Boye et al., 2010; Gledhill, 2012; Hering & Morel, 1990; van den Berg, 1995) as they prevent the formation and adsorption of DFe into/onto particles and decrease the reactivity of Fe species (Bennett et al., 2008). Thus, the presence of ligands mediates the interaction between PFe and DFe in favor of DFe. The formation of unreactive colloidal iron (CFe) could also regulate the stabilization of DFe as it prevents the DFe reactivity with other species or particles (Yücel et al., 2011). It should also be noted that the long residence time of water masses at depth (Figure S10 in Supporting Information S1) should promote the accumulation of DFe near deep vents (Rijkenberg et al., 2018). All these processes could act together to regulate the stabilization of deep hydrothermal iron. However, to our knowledge, the processes governing the stabilization of shallow hydrothermal iron are less well-known and deserve more attention.

Compared to deep vents, a weak dispersion of shallow hydrothermal DFe in the WTSP region is suggested by our data. At LD 5, an almost instantaneous loss of DFe can be observed in the surface layer: 78% of the initial DFe stock is lost over a distance of 600 m between T5 and T4 substations and almost all DFe (97%) is lost over a distance of 16 km between T5 and T1. At LD 10, 47% of the initial DFe input is lost over a 7 km distance between T3 and T2 substations and 85% of DFe is lost at T1. Thus, in contrast to deep iron inputs (Bennett et al., 2008; Fitzsimmons et al., 2014, 2017; Resing et al., 2015), nearly all the DFe supplied by shallow hydrothermal sources appears to be lost over short distances. On a larger scale, away from the arc, surface [DFe] quickly become similar to those measured in Melanesian waters. Only 0.3–0.5 nmol kg<sup>-1</sup> of DFe appears to be stabilized in the photic layer, representing 1%–9% of the initial inputs of LD 5 and LD 10, respectively. An exception is observable for the northern SD 11 for which significant DFe anomalies were measured at surface, possibly due to an impact from New Late'iki.

Thus, DFe from shallow hydrothermalism does not spread as far as that from deeper sources. The oceanic iron cycle is affected by a series of processes that act together to set [DFe] in different parts of the ocean (Boyd et al., 2010). Some chemical processes influencing DFe removal can act in both shallow and deep environments (Johnson et al., 1997; Tagliabue et al., 2019). It is widely accepted that most of DFe is rapidly precipitated near hydrothermal vents due to the rapid mixing of warm, H<sub>2</sub>S-rich, O<sub>2</sub>-poor, low pH fluids with cold, O<sub>2</sub>-rich, high pH seawater (Klevenz et al., 2011; Lilley et al., 2013; Mottl & McConachy, 1990). This causes rapid precipitation of DFe into iron sulfides or rapid oxidation into iron oxyhydroxide precipitates, followed by settling on sediments near the source (Bruland & Lohan, 2006). It is likely to be enhanced in shallow waters due to the higher pH and temperature levels. Iron scavenging can also act in both layers and mediates the removal of DFe by surface adsorption onto sinking particles or by aggregation of CFe (Balistrieri et al., 1981; Goldberg, 1954; Turekian, 1977). This process is also important near the sources of hydrothermal venting where particles are abundant (Tagliabue & Resing, 2016). However, even though this process acts throughout the water column, scavenging is likely enhanced in the particle-rich surface layer as the residence time of DFe relative to scavenging has been reported to be faster in this layer (10–100 days; Black et al., 2020) than at depth (70–270 years; Bergquist & Boyle, 2006; Bruland et al., 1979). In addition, biological activities are likely to produce high levels of biogenic particles and simulations from Beghouri et al. (2019) showed that biogenic particles sink up to two orders of magnitude faster than small inorganic particles. Besides, some processes influencing DFe removal act exclusively in shallow environments that are characterized by higher temperature and pH levels than deeper environments. For example, biological uptake may influence the removal of shallow hydrothermal DFe. Similarly, the photochemical reactivity of organically bound Fe provides an additional removal mechanism for DFe from the surface ocean. The UV portion of the solar spectrum plays a major role in the photoreduction of DFe (Rijkenberg et al., 2003), especially when bound to strong ligands. Light-induced reduction leads to dissociation of stable Fe-L complexes and unreactive colloids (Johnson et al., 1994; Miller et al., 1995). In turn, ligands undergo photo-oxidation and their photodegradation products have a lower conditional stability constant (Barbeau et al., 2003), similar to the weak iron-binding ligand classes (Rue & Bruland, 1995, 1997). This results in less stable iron species and thus ultimately to a DFe loss by scavenging. It should be noted that the short residence time of surface water masses (five times faster current velocity, see Figure S8 in Supporting Information S1 and Section 4.1) implies a faster dilution of DFe near the shallow source, in contrast to deep plumes.

With all these processes in mind and considering a steady state, we developed a simplified budget to semi-quantitatively estimate the fate of hydrothermal DFe (Figure 6a). This budget, based on the evolution of [DFe], considers the processes affecting its distribution vertically (0–200 m) and horizontally over the small-scale LD 5 transect from T5 to T3 (~2 km in total). Estimation of these sinks was possible as [DFe] decreased toward the surface at the three substations. The impact of biological uptake on DFe distribution was accurately quantified from rates measured during the cruise (Lory et al., 2022).

At LD 5-T5, the water column was divided into three sub-boxes representing the (a) upper photic (0–90 m), (b) lower photic (90–150 m), and (c) suboxic (150–200 m) layers. Sub-box (3) was characterized by high [H<sub>2</sub>S] and low pH and [O<sub>2</sub>]. According to the budget, seawater conditions in this layer mainly promoted the precipitation (Lilley et al., 2013) of a significant portion (up to 86%) of hydrothermal DFe into sulfides and/or oxyhydroxides. This estimate is in agreement with those reported in the literature for deep vents (32%–90%; Field & Sherrell, 2000; González-Santana et al., 2020; Lough et al., 2019; Massoth et al., 1998). A vertical flux of 17  $\mu\text{mol DFe m}^{-2} \text{d}^{-1}$  entering the lower photic layer was estimated (see Text S2 in Supporting Information S1 for methodological details). In this layer, precipitation was considered negligible as the environmental conditions may no longer favor this process due to constant pH and [O<sub>2</sub>] and the absence of H<sub>2</sub>S. Scavenging removed a large part of DFe in sub-box (2) (estimated at 9%–63%). Since this wide range was unsatisfying for the budget, this scavenging estimate was finally refined for the sub-box (2) using PFe data (see Text S3 in Supporting Information S1 for methodology of PFe measurements and Table S3 in Supporting Information S1 for PFe data). Obtained scavenging percentages were consistent with those estimated with DFe only, although narrower (40%–72% and 67%–68% in sub-boxes (a) and (b), respectively) and of the same order of magnitude in the two layers. Those scavenging estimates are in good agreement, although slightly higher, with the rare rates reported for hydrothermal systems (~50%; González-Santana et al., 2020). Vertical DFe fluxes into the upper photic layer from the lower photic layer were one order of magnitude lower ( $1.9 \mu\text{mol DFe m}^{-2} \text{d}^{-1}$ ) compared to fluxes from suboxic to lower photic layers but still represented a significant vertical transport of DFe. In this layer (a), biological uptake also has to be considered. Using rates measured during the cruise (9–17  $\text{pmol kg}^{-1} \text{d}^{-1}$ ;

Lory et al., 2022), biological uptake resulted in only 0.7%–3% of DFe removal in the upper photic layer. Adding this biological sink and a scavenging rate similar to the one of the lower photic layer, the budget indicated the need for an additional DFe sink estimated at ~36%.

At LD 5-T4 (~0.6 km from T5), two sub-boxes were considered to discriminate processes acting exclusively in the upper photic layer. Since precipitation in this budget is assumed to be negligible far from the hydrothermal source due to seawater physico-chemical conditions, scavenging is the main process acting in the lower photic layer and was estimated to remove a significant portion of DFe (35%–72%). Biological uptake led to a removal of DFe of 1%–4% (quantified as described above) in the upper photic layer. As for LD 5-T5, an additional DFe sink was estimated to close the budget (13%–29%).

AT LD 5-T3 (~2 km from T5), scavenging was estimated to remove a significant portion of DFe (31%–72%) in the lower photic layer. In the upper photic layer, biological uptake removed 1%–4.3% of DFe and to close the budget, an additional moderate sink removing 14%–24% of DFe was estimated. It should be noted that horizontal fluxes of DFe could not be quantitatively estimated in lack of accurate flow characterization (as discussed in Section 4.1). Qualitatively, however, the southwestern circulation would infer DFe advection from T5 until T3 in all layers; enhanced turbulent surface flow would also favor DFe diffusion within the upper photic layer, from T5 (high [DFe]) to T4 (moderate [DFe]) and then to T3 (low [DFe]). It should be noted that our data prevented us to consider tidally rectified flows and seamount-induced upwellings in this budget although they could strongly shape the distribution of DFe near shallow sources (Lavelle, 2006; Lavelle et al., 2004).

This budget indicates that precipitation, scavenging, and biological uptake appear to act in similar proportion at all substations. In the upper photic layer, biological uptake is a negligible sink in such an iron-rich environment. Scavenging is an important DFe sink in both layers as it removes more DFe from solution (up to 72%) compared with data reported for deep sources (González-Santana et al., 2020). The additional sink of DFe (up to 36%) required to close the budget in the upper photic layer could correspond to a higher scavenging rate in this layer due to the presence of large proportions of biological particles. A portion of this sink could also be due to the photoreduction of organically bound Fe, in agreement with values previously reported in the literature ( $25 \pm 21\%$ ; Kuma et al., 1992). Alternatively, a combination of both processes (scavenging and photoreduction) could also explain this additional DFe loss. Nevertheless, a deeper investigation is necessary to accurately quantify these processes before drawing any conclusions.

It can be noted that T2 and T1 substations were excluded from the budget because no significant [DFe] anomalies were found at these two substations. A clear impact of hydrothermal DFe from T5 was unlikely at these substations, as the main current flow at depth transported the plume southwestward (see Figures 6b and Section 4.1). Nevertheless, the relatively high [DFe] ( $>0.5 \text{ nmol kg}^{-1}$ ) observed at these substations could be due to the influence of other active shallow sources further north of the arc (Baker et al., 2019; German et al., 2006).

DFe from shallow hydrothermal sources does not appear to be transported as far as DFe from deeper sources. This is due to both shorter residence time of surface water masses (a few weeks vs. several months at depth) and physico-chemical conditions in surface waters (pH and temperature). The accumulation of DFe released by shallow hydrothermal sources will therefore be much lower than from sources located at depth. Our results show a negligible effect of biological uptake ( $<5\%$  removal) on DFe distribution. Precipitation is a very important sink for DFe close to the source in the suboxic zone and scavenging seems to act most effectively in the particle-rich surface layer. In addition, one mechanism stabilizing DFe in deep plumes (not discussed in the present study in the absence of data) is DFe complexation with ligands. At shallower depths, photoreduction occurring in the photic layer may instead lead to the dissociation of DFe-stabilizing complexes, releasing inorganic DFe that can then be rapidly scavenged. Therefore, this process must be quantified to conclude on its importance in DFe distribution. Specific surface ocean conditions (dynamics and physico-chemical) preventing DFe accumulation along with chemical and biological processes act together to considerably reduce shallow hydrothermal DFe on a relatively small spatial scale (i.e., a few kilometers). Nevertheless, the cumulative impact of other active shallow sources identified along the Tonga-Kermadec arc (Figure 6b; Baker et al., 2005; De Ronde et al., 2003; Lupton et al., 2004; Massoth et al., 2007), and those likely not identified yet, still impact [DFe] that are higher in the whole Lau Basin compared to [DFe] east of the Tonga arc. Thus, this small but significant fraction of hydrothermal DFe finally stabilized ( $0.3\text{--}0.5 \text{ nmol kg}^{-1}$ ) is able to fertilize the Lau Basin and trigger diazotroph blooms as demonstrated in Bonnet et al. (under review).

## 5. Conclusion

The WTSP Ocean is characterized by the existence of a biogeochemical boundary between its western part, including the Lau Basin and Melanesian waters and characterized by high  $N_2$  fixation, and its eastern part, comprising the western end of the South Pacific gyre and characterized by extremely low diazotrophy rates. Measurements of DFe concentrations in these two subregions confirm that this spatial decoupling of diazotrophy patterns can be explained by the attenuation of Fe limitation west of the Tonga-Kermadec arc. The question of the DFe origin was resolved using the results of an eOMP performed on the cruise transect. By separating the “conservative” component from the DFe section, it was possible to estimate the DFe component coming only from local sources, mostly from hydrothermal sources present in this region. Thus, this study was able to highlight the impact of shallow hydrothermal sources located along the Tonga-Kermadec arc on the DFe cycle of the WTSP Ocean. These sources release a large amount of DFe directly into the surface layer and can fertilize the entire Lau Basin and, to a lesser extent, the Melanesian zone. However, while DFe-rich plumes from deep sources appear to be stabilized and transported in Melanesian waters, DFe from shallow sources persists for only a few tens of kilometers. DFe is indeed lost very rapidly from solution by several physical, chemical, and biological processes such as precipitation and scavenging, some of them acting exclusively in the photic layer such as photoreduction and, to a lesser extent, biological uptake. This weak stabilization of shallow hydrothermal DFe could result in part from the dissociation of DFe-stabilizing complexes and low DFe accumulation mediated by the faster ocean circulation in surface than at depth. Scavenging has also been reported to be more intense in the surface layer, accelerating the removal of shallow hydrothermal iron. Thus, DFe from shallow hydrothermal plumes of the Tonga-Kermadec arc does not appear to be transported over very long distances as previously demonstrated for deep hydrothermal plumes by many studies. However, this small but important fraction of DFe ultimately transported far from the source is sufficient to fertilize the Lau Basin, probably through the cumulative impact of likely many sources located along the Tonga arc. Further analysis of the geochemical differences that may exist between shallow and deep hydrothermal sources and their environment is needed to better understand the stabilization of DFe and other metals in this region. For example, a thorough study of the various ligands released from shallow and deep hydrothermal sources in the region and an assessment of their stability is needed to understand the differences between these two types of hydrothermal systems. An investigation of the behavior of other hydrothermally sourced trace metals could help determine whether the low DFe dispersion observed in shallow hydrothermal environments is a distinct feature of that element or may be observed for other dissolved metals (e.g., DMn), allowing a conclusion to be drawn about the processes involved (i.e., greater dilution or chemical removal specific to DFe). In addition, further sampling of the Lau Basin with finer temporal and/or spatial scales may be necessary for a more thorough study of the dispersion of iron-rich shallow hydrothermal plumes.

### Acknowledgments

We thank the GEOTRACES group for making the dissolved iron transect data available to the public (<http://www.egeotraces.org>), allowing us to define the dissolved iron concentrations of the eOMP water masses presented in this study. We also thank the World Ocean Atlas (Boyer et al., 2018), World Ocean Circulation Experiment (<https://www.ewoce.org/data/index.html>), and Global Ocean Data Analysis Project (Olsen et al., 2020) databases for their extensive hydrographic and biogeochemical data sets used in this study to perform the eOMP analysis. Figures were made using ODV (Schlitzer, 2016). The water mass analysis was performed using the OMP v2.0 MatLab package developed by Johannes Karstensen and Matthias Tomczak (<https://omp.geomar.de/>). LPTE were performed using the Ariane software (<http://www.univ-brest.fr/lpo/ariane>) and the NEMO numerical data set (Gurvan et al., 2019). This work was performed in the framework of the TONGA project (TONGA cruise GEOTRACES GPpr14 November 2019, <https://doi.org/10.17600/18000884>) managed by the LOV (C. Guieu) and the MIO (S. Bonnet) and funded by the TGIR Flotte Océanographique Française, the A-MIDeX of the Aix-Marseille University, the LEFE-CYBER and GMMC program and the ANR. We warmly thank all the scientists, the captain, and the crew of the R/V L'Atalante for their cooperative work at sea. We thank H el ene Planquette for the PFe measurements and for reviewing this study. We thank Sandra Nunige and Elvira Pulido for the processing of nutrient analyses. We thank Lise Artigue for her ingenious idea to couple eOMP and biogeochemical analyses. We warmly thank Joseph Resing and an anonymous referee for their extensive review and for the constructive comments on the manuscript.

### Conflict of Interest

The authors declare no conflicts of interest relevant to this study.

### Data Availability Statement

All data used in this study are available in the supplementary material, with the exception of the nutrient data (nitrate, phosphate, and silicate). All data from the cruise (including nutrients) will be accessible as soon as they are published at <https://www.seanoe.org/data/00770/88169/>.

### References

- Abadie, C., Lacan, F., Radic, A., Pradoux, C., & Poitrasson, F. (2017). Iron isotopes reveal distinct dissolved iron sources and pathways in the intermediate versus deep Southern Ocean. *Proceedings of the National Academy of Sciences*, 114(5), 858–863. <https://doi.org/10.1073/pnas.1603107114>
- Anderson, L. A., & Sarmiento, J. L. (1994). Redfield ratios of remineralization determined by nutrient data analysis. *Global Biogeochemical Cycles*, 8(1), 65–80. <https://doi.org/10.1029/93GB03318>
- Artigue, L., Lacan, F., van Gennip, S., Lohan, M. C., Wyatt, N. J., Woodward, E. M. S., et al. (2020). Water mass analysis along 22°N in the subtropical North Atlantic for the JC150 cruise (GEOTRACES, GApr08). *Deep Sea Research Part I: Oceanographic Research Papers*, 158, 103230. <https://doi.org/10.1016/j.dsr.2020.103230>

- Baker, E. T., Massoth, G. J., Nakamura, K., Embley, R. W., de Ronde, C. E. J., & Arculus, R. J. (2005). Hydrothermal activity on near-arc sections of back-arc ridges: Results from the Mariana trough and Lau Basin: Activity on back-arc ridges. *Geochemistry, Geophysics, Geosystems*, 6(9). <https://doi.org/10.1029/2005GC000948>
- Baker, E. T., Walker, S. L., Massoth, G. J., & Resing, J. A. (2019). The NE Lau Basin: Widespread and abundant hydrothermal venting in the back-arc region behind a superfast subduction zone. *Frontiers in Marine Science*, 6, 382. <https://doi.org/10.3389/fmars.2019.00382>
- Balistreri, L., Brewer, P. G., & Murray, J. W. (1981). Scavenging residence times of trace metals and surface chemistry of sinking particles in the deep ocean. *Deep-Sea Research, Part A: Oceanographic Research Papers*, 28(2), 101–121. [https://doi.org/10.1016/0198-0149\(81\)90085-6](https://doi.org/10.1016/0198-0149(81)90085-6)
- Barbeau, K., Rue, E. L., Trick, C. G., Bruland, K. W., & Butler, A. (2003). Photochemical reactivity of siderophores produced by marine heterotrophic bacteria and cyanobacteria based on characteristic Fe(III) binding groups. *Limnology & Oceanography*, 48(3), 1069–1078. <https://doi.org/10.4319/lo.2003.48.3.1069>
- Baumberger, T., Lilley, M. D., Lupton, J. E., Baker, E. T., Resing, J. A., Buck, N. J., et al. (2020). Dissolved gas and metal composition of hydrothermal plumes from a 2008 submarine eruption on the northeast Lau spreading center. *Frontiers in Marine Science*, 7, 171. <https://doi.org/10.3389/fmars.2020.00171>
- Baumberger, T., Lilley, M. D., Resing, J. A., Lupton, J. E., Baker, E. T., Butterfield, D. A., et al. (2014). Understanding a submarine eruption through time series hydrothermal plume sampling of dissolved and particulate constituents: West Mata, 2008–2012. *Geochemistry, Geophysics, Geosystems*, 15(12), 4631–4650. <https://doi.org/10.1002/2014GC005460>
- Beghoua, H., Gorgues, T., Aumont, O., Planquette, H. F., Tagliabue, A., & Auger, P.-A. (2019). Impact of inorganic particles of sedimentary origin on global dissolved iron and phytoplankton distribution. *Journal of Geophysical Research: Oceans*, 124(12), 8626–8646. <https://doi.org/10.1029/2019JC015119>
- Behrenfeld, M. J., & Milligan, A. J. (2013). Photophysiological expressions of iron stress in phytoplankton. *Annual Review of Marine Science*, 5(1), 217–246. <https://doi.org/10.1146/annurev-marine-121211-172356>
- Bennett, S. A., Achterberg, E. P., Connelly, D. P., Statham, P. J., Fones, G. R., & German, C. R. (2008). The distribution and stabilisation of dissolved Fe in deep-sea hydrothermal plumes. *Earth and Planetary Science Letters*, 270(3–4), 157–167. <https://doi.org/10.1016/j.epsl.2008.01.048>
- Bergquist, B. A., & Boyle, E. A. (2006). Dissolved iron in the tropical and subtropical Atlantic Ocean. *Global Biogeochemical Cycles*, 20(1). <https://doi.org/10.1029/2005GB002505>
- Black, E. E., Kienast, S. S., Lemaitre, N., Lam, P. J., Anderson, R. F., Planquette, H., et al. (2020). Ironing out Fe residence time in the dynamic upper ocean. *Global Biogeochemical Cycles*, 34(9). <https://doi.org/10.1029/2020GB006592>
- Blain, S., Bonnet, S., & Guieu, C. (2008). Dissolved iron distribution in the tropical and sub tropical South Eastern Pacific. *Biogeosciences*, 5(1), 269–280. <https://doi.org/10.5194/bg-5-269-2008>
- Blain, S., Quéguiner, B., Armand, L., Belviso, S., Bombléd, B., Bopp, L., et al. (2007). Effect of natural iron fertilization on carbon sequestration in the Southern Ocean. *Nature*, 446(7139), 1070–1074. <https://doi.org/10.1038/nature05700>
- Bonnet, S., Caffin, M., Berthelot, H., Grosso, O., Benavides, M., Helias-Nunige, S., et al. (2018). In-depth characterization of diazotroph activity across the Western tropical South Pacific hotspot of N<sub>2</sub> fixation (OUTPACE cruise). *Biogeosciences*, 15(13), 4215–4232. <https://doi.org/10.5194/bg-15-4215-2018>
- Bonnet, S., Caffin, M., Berthelot, H., & Moutin, T. (2017). Hot spot of N<sub>2</sub> fixation in the Western tropical South Pacific pleads for a spatial decoupling between N<sub>2</sub> fixation and denitrification. *Proceedings of the National Academy of Sciences*, 114(14), E2800–E2801. <https://doi.org/10.1073/pnas.1619514114>
- Bonnet, S., Guieu, C., Bruyant, F., Prášil, O., Van Wambeke, F., Raimbault, P., et al. (2008). Nutrient limitation of primary productivity in the Southeast Pacific (BIOCOPE cruise). *Biogeosciences*, 5(1), 215–225. <https://doi.org/10.5194/bg-5-215-2008>
- Bonnet, S., Guieu, C., Taillandier, V., Boulart, C., Bouruet-Aubertot, P., Gazeau, F., et al. (under review). Natural iron fertilization by shallow hydrothermal sources fuels diazotroph blooms in the Ocean. [under review].
- Bostock, H. C., Sutton, P. J., Williams, M. J. M., & Opdyke, B. N. (2013). Reviewing the circulation and mixing of Antarctic Intermediate Water in the South Pacific using evidence from geochemical tracers and Argo float trajectories. *Deep Sea Research Part I: Oceanographic Research Papers*, 73, 84–98. <https://doi.org/10.1016/j.dsr.2012.11.007>
- Bowie, A. R., Achterberg, E. P., Mantoura, R. F. C., & Worsfold, P. J. (1998). Determination of sub-nanomolar levels of iron in seawater using flow injection with chemiluminescence detection. *Analytica Chimica Acta*, 361(3), 189–200. [https://doi.org/10.1016/S0003-2670\(98\)00015-4](https://doi.org/10.1016/S0003-2670(98)00015-4)
- Boyd, P. W., Ibsanmi, E., Sander, S. G., Hunter, K. A., & Jackson, G. A. (2010). Remineralization of upper ocean particles: Implications for iron biogeochemistry. *Limnology & Oceanography*, 55(3), 1271–1288. <https://doi.org/10.4319/lo.2010.55.3.1271>
- Boye, M., Nishioka, J., Croot, P., Laan, P., Timmermans, K. R., Strass, V. H., et al. (2010). Significant portion of dissolved organic Fe complexes in fact is Fe colloids. *Marine Chemistry*, 122(1–4), 20–27. <https://doi.org/10.1016/j.marchem.2010.09.001>
- Boyer, T., Garcia, H., Locarnini, R., Zweng, M., Mishonov, A., Reagan, J., et al. (2018). World Ocean Atlas 2018. NOAA National Centers for Environmental Information. Dataset. <https://www.ncei.noaa.gov/archive/accession/NCEI-WOA18%20>
- Bressac, M., Guieu, C., Ellwood, M. J., Tagliabue, A., Wagener, T., Laurenceau-Cornec, E. C., et al. (2019). Resupply of mesopelagic dissolved iron controlled by particulate iron composition. *Nature Geoscience*, 6(12), 995–1000. <https://doi.org/10.1038/s41561-019-0476-6>
- Broecker, W. S. (1974). “NO”, a conservative water-mass tracer. *Earth and Planetary Science Letters*, 23(1), 100–107. [https://doi.org/10.1016/0012-821X\(74\)90036-3](https://doi.org/10.1016/0012-821X(74)90036-3)
- Bruland, K. W., Franks, R. P., Knauer, G. A., & Martin, J. H. (1979). Sampling and analytical methods for the determination of copper, cadmium, zinc, and nickel at the nanogram per liter level in sea water. *Analytica Chimica Acta*, 105, 233–245. [https://doi.org/10.1016/S0003-2670\(01\)83754-5](https://doi.org/10.1016/S0003-2670(01)83754-5)
- Bruland, K. W., & Lohan, M. C. (2006). 02. Controls of trace metals in seawater. *Treatise on Geochemistry*, 6, 23–47.
- Buck, N. J., Resing, J. A., Baker, E. T., & Lupton, J. E. (2018). Chemical fluxes from a recently erupted shallow submarine volcano on the Mariana arc. *Geochemistry, Geophysics, Geosystems*, 19(5), 1660–1673. <https://doi.org/10.1029/2018GC007470>
- Caffin, M., Moutin, T., Foster, R. A., Bouruet-Aubertot, P., Doglioli, A. M., Berthelot, H., et al. (2018). N<sub>2</sub> fixation as a dominant new N source in the Western tropical South Pacific Ocean (OUTPACE cruise). *Biogeosciences*, 15(8), 2565–2585. <https://doi.org/10.5194/bg-15-2565-2018>
- Campbell, L., Carpenter, E., Montoya, J. P., Kustka, A., & Capone, D. G. (2005). Picoplankton community structure within and outside a Trichodesmium bloom in the southwestern Pacific Ocean. *Vie et Milieu*, 55(3), 185–195.
- Cohen, N. R., Noble, A. E., Moran, D. M., McIlvin, M. R., Goepfert, T. J., Hawco, N. J., et al. (2021). Hydrothermal trace metal release and microbial metabolism in the Northeast Lau Basin of the south Pacific Ocean [Preprint]. *Biogeochemistry: Environmental Microbiology*. <https://doi.org/10.5194/bg-2021-96>
- Cutter, G., Casciotti, K., Croot, P., Geibert, W., Heimbürger, L.-E., Lohan, M., et al. (2017). Sampling and Sample-handling Protocols for GEOTRACES Cruises. Version 3. [139pp. & Appendices]. GEOTRACES International Project Office. <https://doi.org/10.25607/OBP-2>



- Davis, R. E. (2005). Intermediate-depth circulation of the Indian and South Pacific oceans measured by autonomous floats. *Journal of Physical Oceanography*, 35(5), 683–707. <https://doi.org/10.1175/JPO2702.1>
- de Ronde, C. E. J., Baker, E. T., Massoth, G. J., Lupton, J. E., Wright, I. C., Feely, R. A., & Greene, R. (2001). Intra-oceanic subduction-related hydrothermal venting, Kermadec volcanic arc, New Zealand. *Earth and Planetary Science Letters*, 193(3–4), 359–369. [https://doi.org/10.1016/S0012-821X\(01\)00534-9](https://doi.org/10.1016/S0012-821X(01)00534-9)
- de Ronde, C. E. J., Massoth, G. J., Lupton, J. E., Baker, B. J., Simmons, S. F., & Graham, I. (2003). Submarine hydrothermal venting related to volcanic arcs. In *Volcanic, geothermal, and ore-forming fluids* (pp. 91–110). Society of Economic Geologists. <https://doi.org/10.5382/SP.10.06>
- Dick, G. J., Anantharaman, K., Baker, B. J., Li, M., Reed, D. C., & Sheik, C. S. (2013). The microbiology of deep-sea hydrothermal vent plumes: Ecological and biogeographic linkages to seafloor and water column habitats. *Frontiers in Microbiology*, 4. <https://doi.org/10.3389/fmicb.2013.00124>
- Dutheil, C., Aumont, O., Gorguès, T., Lorrain, A., Bonnet, S., Rodier, M., et al. (2018). Modelling the processes driving Trichodesmium sp. Spatial distribution and biogeochemical impact in the tropical Pacific Ocean [Preprint]. *Biogeochemistry: Modelling, Aquatic*. <https://doi.org/10.5194/bg-2017-559>
- Field, M. P., & Sherrell, R. M. (2000). Dissolved and particulate Fe in a hydrothermal plume at 9°45'N, East Pacific Rise. *Geochimica et Cosmochimica Acta*, 64(4), 619–628. [https://doi.org/10.1016/S0016-7037\(99\)00333-6](https://doi.org/10.1016/S0016-7037(99)00333-6)
- Fitzsimmons, J. N., Boyle, E. A., & Jenkins, W. J. (2014). Distal transport of dissolved hydrothermal iron in the deep South Pacific Ocean. *Proceedings of the National Academy of Sciences*, 111(47), 16654–16661. <https://doi.org/10.1073/pnas.1418778111>
- Fitzsimmons, J. N., Conway, T. M., Lee, J.-M., Kayser, R., Thyng, K. M., John, S. G., & Boyle, E. A. (2016). Dissolved iron and iron isotopes in the southeastern Pacific Ocean: Southeast Pacific Fe and Fe Isotopes. *Global Biogeochemical Cycles*, 30(10), 1372–1395. <https://doi.org/10.1002/2015GB005357>
- Fitzsimmons, J. N., John, S. G., Marsay, C. M., Hoffman, C. L., Nicholas, S. L., Toner, B. M., et al. (2017). Iron persistence in a distal hydrothermal plume supported by dissolved–particulate exchange. *Nature Geoscience*, 10(3), 195–201. <https://doi.org/10.1038/ngeo2900>
- Ganachaud, A., Cravatte, S., Melet, A., Schiller, A., Holbrook, N. J., Sloyan, B. M., et al. (2014). The Southwest Pacific Ocean circulation and climate experiment (SPICE). *Journal of Geophysical Research: Oceans*, 119(11), 7660–7686. <https://doi.org/10.1002/2013JC009678>
- German, C. R., Baker, E. T., Connelly, D. P., Lupton, J. E., Resing, J., Prien, R. D., et al. (2006). Hydrothermal exploration of the fonalei rift and spreading center and the northeast Lau spreading center. *Geochemistry, Geophysics, Geosystems*, 7(11). <https://doi.org/10.1029/2006GC003124>
- German, C. R., Casciotti, K. A., Dutay, J.-C., Heimbürger, L. E., Jenkins, W. J., Measures, C. I., et al. (2016). Hydrothermal impacts on trace element and isotope ocean biogeochemistry. *Philosophical Transactions of the Royal Society A: Mathematical, Physical & Engineering Sciences*, 374(2081), 20160035. <https://doi.org/10.1098/rsta.2016.0035>
- Gledhill, M. (2012). The organic complexation of iron in the marine environment: A review. *Frontiers in Microbiology*, 3. <https://doi.org/10.3389/fmicb.2012.00069>
- Goldberg, E. D. (1954). Marine geochemistry 1. Chemical scavengers of the sea. *The Journal of Geology*, 62(3), 249–265. <https://doi.org/10.1086/626161>
- González-Santana, D., Planquette, H., Cheize, M., Whitby, H., Gourain, A., Holmes, T., et al. (2020). Processes driving iron and manganese dispersal from the TAG hydrothermal plume (Mid-Atlantic ridge): Results from a GEOTRACES process study. *Frontiers in Marine Science*, 7, 568. <https://doi.org/10.3389/fmars.2020.00568>
- González-Vega, A., Fraile-Nuez, E., Santana-Casiano, J. M., González-Dávila, M., Escánez-Pérez, J., Gómez-Ballesteros, M., et al. (2020). Significant release of dissolved inorganic nutrients from the shallow submarine volcano tagoro (canary islands) based on seven-year monitoring. *Frontiers in Marine Science*, 6, 829. <https://doi.org/10.3389/fmars.2019.00829>
- Guiou, C., & Bonnet, S. (2019). Tonga cruise 2019, L'Atalante R/V. <https://doi.org/10.17600/18000884>
- Guiou, C., Bonnet, S., Petrenko, A., Menkes, C., Chavagnac, V., Desboeufs, K., et al. (2018). Iron from a submarine source impacts the productive layer of the Western Tropical South Pacific (WTSP). *Scientific Reports*, 8(1), 1–9. <https://doi.org/10.1038/s41598-018-27407-z>
- Gurvan, M., Bourdallé-Badie, R., Chanut, J., Clementi, E., Coward, A., Ethé, C., et al. (2019). NEMO ocean engine. <https://doi.org/10.5281/ZENODO.3878122>
- Hawkes, J. A., Connelly, D. P., Rijkenberg, M. J. A., & Achterberg, E. P. (2014). The importance of shallow hydrothermal island arc systems in ocean biogeochemistry. *Geophysical Research Letters*, 41(3), 942–947. <https://doi.org/10.1002/2013GL058817>
- Hering, J. G., & Morel, F. M. M. (1990). Kinetics of trace metal complexation: Ligand-exchange reactions. *Environmental Science & Technology*, 24(2), 242–252. <https://doi.org/10.1021/es00072a014>
- Homoky, W. B., Weber, T., Berelson, W. M., Conway, T. M., Henderson, G. M., van Hulten, M., et al. (2016). Quantifying trace element and isotope fluxes at the ocean–sediment boundary: A review. *Philosophical Transactions of the Royal Society A: Mathematical, Physical & Engineering Sciences*, 374(2081), 20160246. <https://doi.org/10.1098/rsta.2016.0246>
- Hudson, A., Bender, M. L., & Graham, D. W. (1986). Iron enrichments in hydrothermal plumes over the East Pacific Rise. *Earth and Planetary Science Letters*, 79(3–4), 250–254. [https://doi.org/10.1016/0012-821X\(86\)90183-4](https://doi.org/10.1016/0012-821X(86)90183-4)
- IPCC. (Éd.). (2021). *Climate change 2021: The physical science basis. Contribution of working group I to the sixth assessment report of the intergovernmental panel on climate change*. Cambridge University Press.
- John, S. G., & Adkins, J. (2012). The vertical distribution of iron stable isotopes in the North Atlantic near Bermuda. *Global Biogeochemical Cycles*, 26(2). <https://doi.org/10.1029/2011GB004043>
- Johnson, K. S., Coale, K. H., Elrod, V. A., & Tindale, N. W. (1994). Iron photochemistry in seawater from the equatorial Pacific. *Marine Chemistry*, 46(4), 319–334. [https://doi.org/10.1016/0304-4203\(94\)90029-9](https://doi.org/10.1016/0304-4203(94)90029-9)
- Johnson, K. S., Gordon, R. M., & Coale, K. H. (1997). What controls dissolved iron concentrations in the world ocean? *Marine Chemistry*, 57(3–4), 137–161. [https://doi.org/10.1016/S0304-4203\(97\)00043-1](https://doi.org/10.1016/S0304-4203(97)00043-1)
- Klevenz, V., Bach, W., Schmidt, K., Hentscher, M., Koschinsky, A., & Petersen, S. (2011). Geochemistry of vent fluid particles formed during initial hydrothermal fluid-seawater mixing along the Mid-Atlantic Ridge. *Geochemistry, Geophysics, Geosystems*, 12(10). <https://doi.org/10.1029/2011GC003704>
- Kuma, K., Nakabayashi, S., Suzuki, Y., Kudo, I., & Matsunaga, K. (1992). Photo-reduction of Fe(III) by dissolved organic substances and existence of Fe(II) in seawater during spring blooms. *Marine Chemistry*, 37(1–2), 15–27. [https://doi.org/10.1016/0304-4203\(92\)90054-E](https://doi.org/10.1016/0304-4203(92)90054-E)
- Labatut, M. (2014). Apports continentaux de Fer à l'océan: Approche isotopique—Océan Pacifique Equatorial [Océan, Atmosphère, Université Toulouse III Paul Sabatier]. tel-01128617.
- Landing, W. M., Haraldsson, C., & Paxeus, N. (1986). Vinyl polymer agglomerate based transition metal cation-chelating ion-exchange resin containing the 8-hydroxyquinoline functional group. *Analytical Chemistry*, 58(14), 3031–3035. <https://doi.org/10.1021/ac00127a029>
- Lavelle, J. W. (2006). Flow, hydrography, turbulent mixing, and dissipation at Fieberling Guyot examined with a primitive equation model. *Journal of Geophysical Research*, 111(C7), C07014. <https://doi.org/10.1029/2005JC003224>

- Lavelle, J. W., Lozovatsky, I. D., & Smith, D. C. (2004). Tidally induced turbulent mixing at irving seamount-modeling and measurements: Tidally induced turbulent mixing. *Geophysical Research Letters*, *31*(10). <https://doi.org/10.1029/2004GL019706>
- Lilley, M. D., Feely, R. A., & Trefry, J. H. (2013). Chemical and biochemical transformations in hydrothermal plumes. In *Seafloor hydrothermal systems: Physical, chemical, biological, and geological interactions* (pp. 369–391). American Geophysical Union (AGU). <https://doi.org/10.1029/GM091p0369>
- Lory, C., Van Wambeke, F., Fourquez, M., Berman-Frank, I., Barani, A., Tilliette, C., et al. (2022). Assessing the contribution of diazotrophs to microbial Fe uptake using a group specific approach in the Western Tropical South Pacific Ocean. *ISME COMMUN*, *2*(1), 41. <https://doi.org/10.1038/s43705-022-00122-7>
- Loscher, B. M., De Baar, H. J. W., De Jong, J. T. M., Veth, C., & Dehairs, F. (1997). The distribution of Fe in the Antarctic circumpolar current. *Deep Sea Research Part II: Topical Studies in Oceanography*, *44*(1–2), 143–187. [https://doi.org/10.1016/S0967-0645\(96\)00101-4](https://doi.org/10.1016/S0967-0645(96)00101-4)
- Lough, A. J. M., Homoky, W. B., Connelly, D. P., Comer-Warner, S. A., Nakamura, K., Abyaneh, M. K., et al. (2019). Soluble iron conservation and colloidal iron dynamics in a hydrothermal plume. *Chemical Geology*, *511*, 225–237. <https://doi.org/10.1016/j.chemgeo.2019.01.001>
- Lupton, J. E., Arculus, R. J., Resing, J., Massoth, G. J., Greene, R. R., Evans, L. J., & Buck, N. (2012). Hydrothermal activity in the north-west Lau backarc basin: Evidence from water column measurements. *Geochemistry, Geophysics, Geosystems*, *13*, Q0AF04. <https://doi.org/10.1029/2011GC003891>
- Lupton, J. E., Pyle, D. G., Jenkins, W. J., Greene, R., & Evans, L. (2004). Evidence for an extensive hydrothermal plume in the Tonga-Fiji region of the South Pacific. *Geochemistry, Geophysics, Geosystems*, *5*(1). <https://doi.org/10.1029/2003GC000607>
- Mahadevan, A. (2016). The impact of submesoscale physics on primary productivity of plankton. *Annual Review of Marine Science*, *8*(1), 161–184. <https://doi.org/10.1146/annurev-marine-010814-015912>
- Martin, J. H. (1990). Glacial-interglacial CO<sub>2</sub> change: The iron hypothesis. *Paleoceanography*, *5*(1), 1–13. <https://doi.org/10.1029/PA005i001p00001>
- Martin, J. H., Coale, K. H., Johnson, K. S., Fitzwater, S. E., Gordon, R. M., Tanner, S. J., et al. (1994). Testing the iron hypothesis in ecosystems of the equatorial Pacific Ocean. *Nature*, *371*(6493), 123–129. <https://doi.org/10.1038/371123a0>
- Massoth, G., Baker, E., Worthington, T., Lupton, J., de Ronde, C., Arculus, R., et al. (2007). Multiple hydrothermal sources along the south Tonga arc and Valu Fa Ridge. *Geochemistry, Geophysics, Geosystems*, *8*(11). <https://doi.org/10.1029/2007GC001675>
- Massoth, G. J., Baker, E. T., Feely, R. A., Lupton, J. E., Collier, R. W., Gendron, J. F., et al. (1998). Manganese and iron in hydrothermal plumes resulting from the 1996 Gorda Ridge Event. *Deep Sea Research Part II: Topical Studies in Oceanography*, *45*(12), 2683–2712. [https://doi.org/10.1016/S0967-0645\(98\)00089-7](https://doi.org/10.1016/S0967-0645(98)00089-7)
- Menard, H. (1960). the East Pacific Rise. *Science*, *132*(3441), 1737–1746. <https://doi.org/10.1126/science.132.3441.1737>
- Miller, W. L., King, D. W., Lin, J., & Kester, D. R. (1995). Photochemical redox cycling of iron in coastal seawater. *Marine Chemistry*, *50*(1–4), 63–77. [https://doi.org/10.1016/0304-4203\(95\)00027-0](https://doi.org/10.1016/0304-4203(95)00027-0)
- Mills, M. M., Ridame, C., Davey, M., La Roche, J., & Geider, R. J. (2004). Iron and phosphorus co-limit nitrogen fixation in the eastern tropical North Atlantic. *Nature*, *429*(6989), 292–294. <https://doi.org/10.1038/nature02550>
- Morris, P. J., & Charette, M. A. (2013). A synthesis of upper ocean carbon and dissolved iron budgets for Southern Ocean natural iron fertilisation studies. *Deep Sea Research Part II: Topical Studies in Oceanography*, *90*, 147–157. <https://doi.org/10.1016/j.dsr2.2013.02.001>
- Mottl, M. J., & McConachy, T. F. (1990). Chemical processes in buoyant hydrothermal plumes on the East Pacific Rise near 21°N. *Geochimica et Cosmochimica Acta*, *54*(7), 1911–1927. [https://doi.org/10.1016/0016-7037\(90\)90261-I](https://doi.org/10.1016/0016-7037(90)90261-I)
- Moutin, T., & Bonnet, S. (2015). OUTPACE cruise, L'Atalante R/V. <https://doi.org/10.17600/15000900>
- Moutin, T., Karl, D. M., Duhamel, S., Rimmelin, P., Raimbault, P., Van Mooy, B. A. S., & Claustre, H. (2008). Phosphate availability and the ultimate control of new nitrogen input by nitrogen fixation in the tropical Pacific Ocean. *Biogeosciences*, *5*(1), 95–109. <https://doi.org/10.5194/bg-5-95-2008>
- Obata, H., Karatani, H., & Nakayama, E. (1993). Automated determination of iron in seawater by chelating resin concentration and chemiluminescence detection. *Analytical Chemistry*, *65*(11), 1524–1528. <https://doi.org/10.1021/ac00059a007>
- Olsen, A., Lange, N., Key, R. M., Tanhua, T., Bittig, H. C., Kozyr, A., et al. (2020). An updated version of the global interior ocean biogeochemical data product, GLODAPv2.2020. *Earth System Science Data*, *12*(4), 3653–3678. <https://doi.org/10.5194/essd-12-3653-2020>
- Peters, B. D., Jenkins, W. J., Swift, J. H., German, C. R., Moffett, J. W., Cutter, G. A., et al. (2018). Water mass analysis of the 2013 US GEOTRACES eastern Pacific zonal transect (GP16). *Marine Chemistry*, *201*, 6–19. <https://doi.org/10.1016/j.marchem.2017.09.007>
- Plank, S., Marchese, F., Genzano, N., Nolde, M., & Martinis, S. (2020). The short life of the volcanic island New Late'iki (Tonga) analyzed by multi-sensor remote sensing data. *Scientific Reports*, *10*(1), 22293. <https://doi.org/10.1038/s41598-020-79261-7>
- Pollard, R., Sanders, R., Lucas, M., & Statham, P. (2007). The crozet natural iron bloom and export experiment (CROZEX). *Deep Sea Research Part II: Topical Studies in Oceanography*, *54*(18–20), 1905–1914. <https://doi.org/10.1016/j.dsr2.2007.07.023>
- Raapoto, H., Martinez, E., Petrenko, A., Doglioli, A., Gorgues, T., Sauzède, R., et al. (2019). Role of iron in the marquesas island mass effect. *Journal of Geophysical Research: Oceans*, *124*(11), 7781–7796. <https://doi.org/10.1029/2019JC015275>
- Raven, J. A., Evans, M. C. W., & Korb, R. E. (1999). The role of trace metals in photosynthetic electron transport in O<sub>2</sub>-evolving organisms. *Photosynthesis Research*, *60*(2–3), 111–150. <https://doi.org/10.1023/A:1006282714942>
- Redfield, A. C., Ketchum, B. H., & Richards, F. A. (1963). The influence of organisms on the composition of sea-water. In *The composition of seawater: Comparative and descriptive oceanography* (Vol. 2, pp. 26–77). Interscience Publishers.
- Reid, J. L. (1997). On the total geostrophic circulation of the Pacific ocean: Flow patterns, tracers, and transports. *Progress in Oceanography*, *39*(4), 263–352. [https://doi.org/10.1016/S0079-6611\(97\)00012-8](https://doi.org/10.1016/S0079-6611(97)00012-8)
- Resing, J. A., Baker, E. T., Lupton, J. E., Walker, S. L., Butterfield, D. A., Massoth, G. J., & Nakamura, K. (2009). Chemistry of hydrothermal plumes above submarine volcanoes of the Mariana arc: Hydrothermal plume chemistry of the Mariana arc. *Geochemistry, Geophysics, Geosystems*, *10*(2). <https://doi.org/10.1029/2008GC002141>
- Resing, J. A., Sedwick, P. N., German, C. R., Jenkins, W. J., Moffett, J. W., Sohst, B. M., & Tagliabue, A. (2015). Basin-scale transport of hydrothermal dissolved metals across the South Pacific Ocean. *Nature*, *523*(7559), 200–203. <https://doi.org/10.1038/nature14577>
- Rijkenberg, M. J. A., Gerringa, L. J. A., Timmermans, K. J., Fischer, A. C., Carolus, V., Maas, L. R. M., et al. (2003). *The photoreduction of iron in seawater*. EGS - AGU - EUG Joint Assembly.
- Rijkenberg, M. J. A., Slagter, H. A., Rutgers van der Loeff, M., van Ooijen, J., & Gerringa, L. J. A. (2018). Dissolved Fe in the deep and upper arctic ocean with a focus on Fe limitation in the nansen basin. *Frontiers in Marine Science*, *5*, 88. <https://doi.org/10.3389/fmars.2018.00088>
- Rousselet, L., de Verneil, A., Doglioli, A. M., Petrenko, A. A., Duhamel, S., Maes, C., & Blanke, B. (2018). Large-to submesoscale surface circulation and its implications on biogeochemical/biological horizontal distributions during the OUTPACE cruise (southwest Pacific). *Biogeosciences*, *15*(8), 2411–2431. <https://doi.org/10.5194/bg-15-2411-2018>

- Rudnick, R. L., & Gao, S. (2003). Composition of the continental crust. In *Treatise on geochemistry* (pp. 1–64). Elsevier. <https://doi.org/10.1016/B0-08-043751-6/03016-4>
- Rue, E. L., & Bruland, K. W. (1995). Complexation of iron(III) by natural organic ligands in the Central North Pacific as determined by a new competitive ligand equilibration/adsorptive cathodic stripping voltammetric method. *Marine Chemistry*, *50*(1–4), 117–138. [https://doi.org/10.1016/0304-4203\(95\)00031-L](https://doi.org/10.1016/0304-4203(95)00031-L)
- Rue, E. L., & Bruland, K. W. (1997). The role of organic complexation on ambient iron chemistry in the equatorial Pacific Ocean and the response of a mesoscale iron addition experiment. *Limnology & Oceanography*, *42*(5), 901–910. <https://doi.org/10.4319/lo.1997.42.5.0901>
- Sander, S. G., & Koschinsky, A. (2011). Metal flux from hydrothermal vents increased by organic complexation. *Nature Geoscience*, *4*(3), 145–150. <https://doi.org/10.1038/ngeo1088>
- Santana-Casiano, J. M., González-Dávila, M., Fraile-Nuez, E., de Armas, D., González, A. G., Domínguez-Yanes, J. F., & Escánez, J. (2013). The natural ocean acidification and fertilization event caused by the submarine eruption of El Hierro. *Scientific Reports*, *3*(1), 1140. <https://doi.org/10.1038/srep01140>
- Schlitzer, R. (2016). Ocean Data View. Retrieved from <https://odv.awi.de>
- Shiozaki, T., Kodama, T., & Furuya, K. (2014). Large-scale impact of the island mass effect through nitrogen fixation in the Western South Pacific Ocean. *Geophysical Research Letters*, *41*(8), 2907–2913. <https://doi.org/10.1002/2014GL059835>
- Stoffers, P., Worthington, T. J., Schwarz-Schampera, U., Hannington, M. D., Massoth, G. J., Hekinian, R., et al. (2006). Submarine volcanoes and high-temperature hydrothermal venting on the Tonga arc, southwest Pacific. *Geology*, *34*(6), 453. <https://doi.org/10.1130/G22227.1>
- Sunda, W. G., & Huntsman, S. A. (1995). Iron uptake and growth limitation in oceanic and coastal phytoplankton. *Marine Chemistry*, *50*(1–4), 189–206. [https://doi.org/10.1016/0304-4203\(95\)00035-P](https://doi.org/10.1016/0304-4203(95)00035-P)
- Tagliabue, A., Bopp, L., Dutay, J.-C., Bowie, A. R., Chever, F., Jean-Baptiste, P., et al. (2010). Hydrothermal contribution to the oceanic dissolved iron inventory. *Nature Geoscience*, *3*(4), 252–256. <https://doi.org/10.1038/ngeo818>
- Tagliabue, A., Bowie, A. R., De Vries, T., Ellwood, M. J., Landing, W. M., Milne, A., et al. (2019). The interplay between regeneration and scavenging fluxes drives ocean iron cycling. *Nature Communications*, *10*(1), 4960. <https://doi.org/10.1038/s41467-019-12775-5>
- Tagliabue, A., Mtshali, T., Aumont, O., Bowie, A. R., Klunder, M. B., Roychoudhury, A. N., & Swart, S. (2012). A global compilation of dissolved iron measurements: Focus on distributions and processes in the Southern Ocean. *Biogeosciences*, *9*(6), 2333–2349. <https://doi.org/10.5194/bg-9-2333-2012>
- Tagliabue, A., & Resing, J. (2016). Impact of hydrothermalism on the ocean iron cycle. *Philosophical Transactions of the Royal Society A: Mathematical, Physical & Engineering Sciences*, *374*(2081), 20150291. <https://doi.org/10.1098/rsta.2015.0291>
- Talley, L. D., Pickard, G. L., & Emery, W. J. (Eds.). (2011). *Descriptive physical oceanography: An introduction* (6th ed.). Academic Press.
- Talley, L. D., Sparrow, M., Chapman, P., & Gould, J. (2007). *Pacific Ocean*. National Oceanography Center.
- Tarasov, V. G. (2006). Effects of shallow-water hydrothermal venting on biological communities of coastal marine ecosystems of the Western Pacific. *Advances in Marine Biology*, *50*, 267–421. Elsevier. [https://doi.org/10.1016/S0065-2881\(05\)50004-X](https://doi.org/10.1016/S0065-2881(05)50004-X)
- Tomczak, M. (1999). Some historical, theoretical and applied aspects of quantitative water mass analysis. *Journal of Marine Research*, *57*(2), 275–303. <https://doi.org/10.1357/002224099321618227>
- Tomczak, M., & Godfrey, J. S. (2003). *Regional oceanography: An introduction* (p. 2). Daya Publ. House.
- Tomczak, M., & Large, D. G. B. (1989). Optimum multiparameter analysis of mixing in the thermocline of the eastern Indian Ocean. *Journal of Geophysical Research*, *94*(C11), 16141. <https://doi.org/10.1029/JC094iC11p16141>
- Turekian, K. K. (1977). The fate of metals in the oceans. *Geochimica et Cosmochimica Acta*, *41*(8), 1139–1144. [https://doi.org/10.1016/0016-7037\(77\)90109-0](https://doi.org/10.1016/0016-7037(77)90109-0)
- van den Berg, C. M. G. (1995). Evidence for organic complexation of iron in seawater. *Marine Chemistry*, *50*(1–4), 139–157. [https://doi.org/10.1016/0304-4203\(95\)00032-M](https://doi.org/10.1016/0304-4203(95)00032-M)
- Von Damm, K. L. (1990). Seafloor hydrothermal activity: Black smoker chemistry and chimneys. *Annual Review of Earth and Planetary Sciences*, *18*(1), 173–204. <https://doi.org/10.1146/annurev.ea.18.050190.001133>
- Webb, D. J. (2000). Evidence for shallow zonal jets in the south equatorial current region of the Southwest Pacific. *Journal of Physical Oceanography*, *30*(4), 706–720. [https://doi.org/10.1175/1520-0485\(2000\)030<0706:EFSZJ>2.0.CO;2](https://doi.org/10.1175/1520-0485(2000)030<0706:EFSZJ>2.0.CO;2)
- Wu, J., Wells, M. L., & Rember, R. (2011). Dissolved iron anomaly in the deep tropical–subtropical Pacific: Evidence for long-range transport of hydrothermal iron. *Geochimica et Cosmochimica Acta*, *75*(2), 460–468. <https://doi.org/10.1016/j.gca.2010.10.024>
- Yücel, M., Gartman, A., Chan, C. S., & Luther, G. W. (2011). Hydrothermal vents as a kinetically stable source of iron-sulphide-bearing nanoparticles to the ocean. *Nature Geoscience*, *4*(6), 367–371. <https://doi.org/10.1038/ngeo1148>
- Zhurbas, V., & Oh, I. S. (2004). Drifter-derived maps of lateral diffusivity in the Pacific and Atlantic Oceans in relation to surface circulation patterns. *Journal of Geophysical Research*, *109*(C5), C05015. <https://doi.org/10.1029/2003JC002241>